Biomechanical modeling of deglutition

Nicolás Ramírez Parra

Universidad del Valle
Faculty of Engineering, School of Mechanical Engineer
Cali, Colombia
2018

Biomechanical Modeling of Deglutition

Nicolás Ramírez Parra

Thesis submitted as a partial requirement to apply for the degree of:
Magister in Mechanical Engineering

Supervisors:
MSc., Jair Ladino
Ph.D., Nicolás Hermant

Line of Research:
Biofluidics and Computational Fluid Dynamics
Research Group:
Fatigue and Surfaces (GIFS)

Universidad del Valle
Faculty of Engineering, School of Mechanical Engineer
Cali, Colombia
2018

To my family

Either we shall find what it is we are seeking or at least we shall free ourselves from the persuasion that we know what we do not know.

Plato, The Republic

Acknowledgments

I acknowledge that this work was sponsored by the Project "Biomode: Biomechanical Modiling of Deglutition". This project was a collaboration between the Universidad del Valle and University of Grenoble, and had the support of Colciencias with the internal code C.I. 2864. A special mention to the professors Jair Ladino, Fernando Casanova and Nicolas Hermant who actively contributed to the results of this work. As well as the professors from University of Grenoble, Yohan Payan and Pascal Perrier, who guided us with valuable advice.

Additionally, we thank the collaboration from Mathieu Labrunie, Pierre Badin (GIPSA lab, Grenoble, France) and Laurent Lamalle (IRMaGe, Grenoble, France) whom provided the MRI data and articulatory contours.

Abstract

Swallowing is a physiological process whose malfunction affects the human quality of life, e.g. malnutrition, dehydration or asphyxia, and has been studied using *in vivo* approaches. However, advances in computational capacity have encouraged the production of more accurate computational models offering advantages such as flexibility and reduced experimental costs. Hence, this work proposed the numerical solution of a 2D sagittal swallowing model with physiological accurate tongue's dorsum dynamics based on real time magnetic resonance imaging (RT-MRI) of a healthy young adult. The work designed a full factorial set of simulations and with a second order Box Behnken' surface response design, dimensional relationships were established between food bolus' rheology, swallowing speed, output flow rate, force and shear force over the tongue. Moreover, a dimensionless model was also proposed and exponential behaviors of pressure and friction coefficients as a function of Reynolds number were found with an exponential relationship. Such results are intended to predict swallowing flow conditions based on bolus' rheology and the speed of the swallowing event, and also serve as a first validation for more complex models that use other representation techniques. As validation approaches, the work addressed three indirect validations. First, a comparison with food bolus' centroid motion extracted from RT-MRI with image processing techniques from where a first validation of the order of magnitude was issued. Then, a comparison with simpler geometries of squeezing flow with similar results in normal force and shear force over the tongue's surface. And finally, and comparison with an experimental bench of oral swallowing using particle image velocimetry (PIV) technique, which was designed and constructed and showed similar order of magnitudes with respect to simulations with the same geometry.

Keywords: swallowing, computational fluid dynamics, modeling, food bolus, rheology.

Content

List of Figures

List of Tables

List of symbols

Symbols with Latin letters

Symbol	Term	SI unit	First Appearance
K	Flow consistency index	$Pa \cdot s^n$	2.2.2
$\mathbf{X}$	Vectorial function of the tongue's contour	mm	3.1.1
N	Number of points of spatial discretization for x	1	3.1.1
M	Number of points of spatial discretization for y	1	3.1.1
P	Number of points of temporal discretization for x	1	3.1.1
Q	Number of points of temporal discretization for y	1	3.1.1
$\mathbf{u}$	field of velocities	mm/s	3.1.3
P	Pressure field	Pa	3.1.3
S_ϕ	Sources	Pa	3.1.3
H_0	Distance between tongue and palate boudary	mm	3.1.3
A_t	Face Area magnitude	m^2/m	3.1.5
Q_{outlet}	Volume flow rate	$m^3/s/m$	3.1.5
v_{outlet}	Velocity magnitude	m/s	3.1.5
F_t	Static pressure force	N/m	3.1.5
Δt	Time step	s	3.2.4
t_e	Time of event	s	3.1.5

Greek letter symbols

Symbol	Term	SI unit	First Appearance
ρ	Density	$kg \cdot m^{-3}$	2.2.2
μ	Dynamic viscosity	$Pa \cdot s$	*Sec.*2.2.2
η	Kinematic viscosity	m^2/s	*Sec.*2.2.2
ϕ_i	Field variables	$-$	*Sec.*3.1.5
τ_t	Wall shear force	N/m	*Sec*3.1.5

Subindex

Subindex	Term
i	index counter
j	index counter
k	index counter
l	index counter

Superscript

Subindex	Term
n	Flow behavior index
i	index counter
j	index counter
k	index counter
l	index counter

Abbreviation

Abbreviation	Term
RT-MRI	Real time magnetic resonance imaging
PIV	Particle image velocimetry
FSI	Fluid structure interaction

Abbreviation	**Term**
2D	Two dimensional
3D	Three dimensional
LES	Lower esophageal sphincter
UES	Upper esophageal sphincter
CFD	Computational fluid dynamics
GPJ	Glossopalatal junction
FEM	Finite Element Methods
IB	Immersed boundary
SPH	Smoothed particle hydrodynamics
LSM	Least Square Method
IB	Immersed boundary
ATR	Active tongue region
UDF	User Defined Function
DOE	Design of experiments

Introduction

The swallowing process, also known as deglutition, is a physiological process in which several organs, consisting of different kinds of tissue, transport the food bolus from the oral cavity to the low esophageal sphincter by its coordinated interaction [30]. Any physiological or pathological affection to the normal swallowing is known as dysphagia [58].

There are risk factors in the incidence of dysphagia such as age and degenerative neurological conditions, such as stroke survivors, individuals with Parkinson disease or multiple sclerosis, as well as head and neck cancer[1]. Therefore, it is not surprising that developed countries actively research age-related diseases, such as dysphagia, since the demographic behavior tends toward an elder population. In response, research faculties and projects have been created around the world, such as the "Dysphagia Reasearch society[1]" and "eSwallHome[2]". In a similar manner, dysphagia has drawn the attention of the health and nutrition industry, which is exploring new product lines, specifically targeting dysphagic individuals, such as *ThickenUp Clear*, from Nestlé Health Science [41].

Even though dysphagia is gaining relevance among our modern society, the mechanisms of swallowing itself are not fully understood. Therefore, several researches have focused their attention in swallowing physics by taken one or several of the following study approaches: *in-vivo*, *in-silico* and/or *in-vitro*. The main topics of these studies have been the comparison of swallowing parameters among populations (e.g. Young vs Adults [46] or Female vs Male [56]), the characterization of rheological properties of common boluses [6, 3, 22] or the description of mechanical properties of tissues involved [15], among others.

The study approaches have strengths and weaknesses. For example, most of the *in-vivo* studies report subjects with diverse anthropometry and physiology, and consequently the variety of factors may lead to spurious correlations or hinder the comparison among studies. In this sense, parametric *in-silico* approaches are better suited to establish correlations among several physical variables, since there is the possibility to change the parameters of the model

[1] http://www.dysphagiaresearch.org
[2] http://www.agence-nationale-recherche.fr/Project-ANR-13-TECS-0011

without altering another variable or threatening the subjects' wellbeing, but these studies most certainly lost physiological accuracy due to simplifications in the mathematical description. Therefore the approaches are complementary and the data they gather contribute to a better understanding of the physics of this physiological process. Such knowledge would enable the design of bolus thickeners, therapeutic procedures, surgery procedures, prostheses, etc., all of them intended to improve the life quality of people affected by dysphagia [59], [24], [47].

To describe the swallowing process from a rigorous physical point of view, the elastic behavior of the tissues and the fluid mechanics of the food bolus, as well as its fluid-structure interaction (FSI) should be considered. On one side, since the tissues in the oropharyngeal tract are mostly connective tissues, they are expected to be in general anisotropic, nonlinear-elastic, non-homogeneous (fiber-orientation dependent) and viscoelastic with large deformations, as any other biological tissue [14]. On the other side, from the fluid mechanics and rheological perspective, the food bolus can be linear, non-linear, semi-solid, viscoelastic fluid, whose properties may depend on temperature, time and shear-rate [43, 2].

However, it is important to first simplify the physical description and then create models with increasing complexity and physiological accuracy. In this sense, the aim of this work was to develop a 2D sagittal *in-silico* model of the bolus' fluid dynamics, which is driven by a physiological-accurate motion of the tongue's *dorsum* during the oral phase of swallowing of a healthy human adult.

To this end the first part of this work, **Chapter 2**, presents some remarks on background knowledge in swallowing anatomy and physiology, the swallowing stages, with a particular interest in the oral phase. Additionally, it summarizes the state of the art of *in-silico* and *in-vitro* studies that model one or several swallowing stages with different levels of physiological accuracy. Special emphasis was made on simplifications and methods used in the mathematical description and solution, which served as guidelines to propose a novel *in-silico* model and validation approaches.

Later, **Chapter 3** describes the construction of the novel physiological-accurate *in-silico* model of oral swallowing. This chapter describes the geometry of the oral cavity, the dynamics of the tongue's motion and the governing equations, assumptions and simplifications of the fluid mechanics of swallowing. Later on, a series of simulations with different input variables (rheology and event time) is proposed to study the response in time of variables of interest (flow rate, output velocity, force and shear rate over the tongue), and quantify the incidence of the input variables and relations among them using a quadratic Box-Behnkens design. Finally, this chapter also describes the construction of a dimensionless model, which relates force and shear coefficients with a mean Reynolds number for each case.

In order to validate the orders of magnitude in the previous chapters, several validation approaches are proposed in **Chapter 4**. First, the mean velocity of the centroid of the food bolus is tracked frame by frame in an *in-vivo* procedure and then compared to the one predicted by the model. Second, two additional *in-silico* models with simpler geometries are presented, where one of them also coincides with a geometry proposed in literature. Third, a novel experimental bench of oral swallowing is presented and also used as indirect validation.

Finally, **Chapter 5** concludes the results discussed in previous chapters and list a series of recommendations and possible future works that can be derived from this study.

State of the Art

Contents

2.1 The swallowing process

Swallowing is defined broadly as a physiological process where several biological structures transport the food bolus from the oral cavity to the lower esophageal sphincter (LES) by its coordinated interaction [30].

The Figure **2-1** shows the main biological structures of the oral cavity in a sagittal plane. It encompasses everything after the labial seal, the teeth and the gingivae (plural for gingiva), and is constrained by the hard and soft palates, the tongue and the mucous membrane that connects the tongue with the inner part of the mandible [19]. Additionally, it also shows the tongue's *dorsum* and apex. Following the oral cavity, comes the pharynx and esophagus, which are constrained by the Upper Esophageal Sphincter (UES) and LES, as seen in Figure **2-1**.

The swallowing process is artificially subdivided in swallowing stages known as preparatory, oral, pharyngeal and esophageal stages. In the preparatory stage the process begins and the food is introduced in the oral cavity; this stage involves labial seal, buccal and facial tone and mastication, as is further detailed in [30]. Moreover, saliva also plays a key role at this

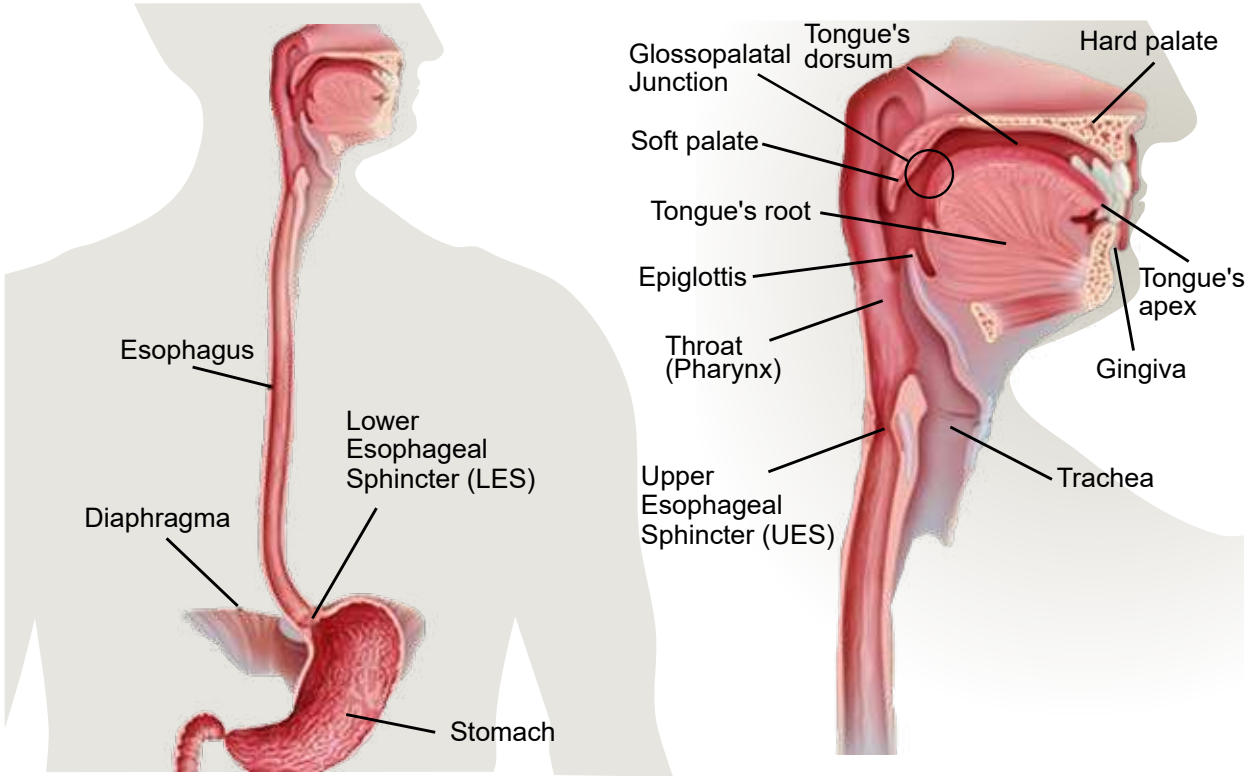

Figure 2-1: Graphical representation of the oral cavity from a sagittal plane. Source: Modified from [12].

stage, pre-digesting and lubricating the food. As a result of this stage, the ingested food and liquids are transformed into a fluid known as food bolus.

After bolus creation, the oral propulsive stage begins. The tongue's apex makes contact with the hard palate and then the tongue's *dorsum* begins to elevate in a peristalic manner, transporting the bolus to the oropharynx [42]. This movement involves complex muscle coordination in order to achieve a well formed and positioned bolus, ready for the next stage without premature leakage into the pharynx [43].

In the pharyngeal stage, the food bolus is transported through the pharynx into the esophagus. Through the pharynx flows air and food bolus, while respiration and swallowing. If they were to flow simultaneously, it would carry severe health consequences, therefore coordination of the biological structures is essential [35].

Finally, in the esophageal stage, comprised between the UES and the LES, the food moves caudally in the esophagus toward the stomach, see Figure **2-1**. This movement is called peristalsis and is defined as a coordinated pattern of muscle contractions and relaxation that describes a wave-like activity [38].

2.2 In-silico models of swallowing classified by stage

As stated before, is common practice to artificially divide the swallowing process in four stages of swallowing known as preparatory, propulsive, pharyngeal and esophageal stages. Since the physics of the preparatory stage differs substantially from the other stages, it is excluded in this work and would require a review on its own. Moreover, the models from literature in the following sections assumed a completely formed bolus.

2.2.1 Propulsive stage

The propulsive stage, or oral stage, has been traditionally studied using videofluoroscopic techniques [34], however some analytic and numerical models have also been proposed.

The most basic model was proposed by Nicosia et al. in [42], whose model's mathematical background was based on the rheological model of a squeezing flow between two plates by Weinbaum et al in [50]. The model consists of a simplified axisymmetric geometry of two circular plates, with a fluid gap between them. When the inferior rigid plate is pushed upward and the fluid in-between is propelled outward radially as would occur to the bolus in the oropharynx, as depicted in Figure **2-2**. This work built a dimensionless model that related the effect of bolus' rheological properties and the applied lingual pressure to

the dynamics of bolus ejection. The study identified three regimes: for viscosity $< 100cP$ the density (inertial) variation dominates the bolus dynamics, for viscosity between 100 to $1000cP$ the density and viscosity effects were similar and for viscosity over $1000cP$ the viscosity dominates. Therefore, they concluded that density, and not only viscosity, affects the bolus transit [42].

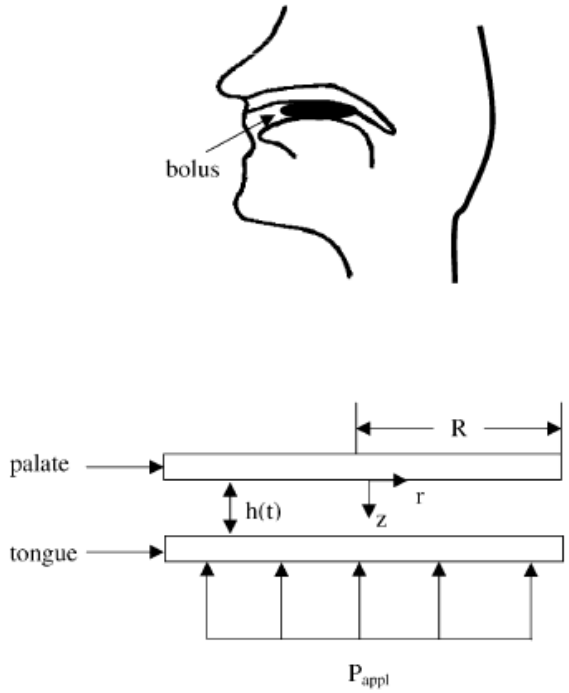

Figure 2-2: Two-dimensional axisymetric model by [42]. Source: Taken from [42].

Nicosia et al. later complemented this model to include the partial-slip condition associated with saliva in [44]. The model considered a thin lubricating layer expected between the bolus and the tongue, and its objective was to determine the shear rate as a function of the relative degree of boundary slip and varying viscosity of several Newtonian boluses. It was found that the viscosity and lubrication level, among other factors, strongly affect shear rate, and furthermore, the assumption a single shear rate for the oral fluid mechanics may be too simplistic.

With a similar approach, Mossaz et al. in [40] described the food bolus propagation between the tongue and the palate using two parallel plates that squeeze a fluid in-between, but this time the fluid had free surfaces and planar symmetry was assumed. The objective of the study was to describe the release mechanism for sensory stimuli of the food molecules. This was done by modeling how the food bolus spreads on the tongue. One of its highlights was

the comparison with a *in-vivo* spreading test, where the spreading area of the bolus was measured.

A variation of this geometry is proposed by Fairfield in [10], where the boundary that represented the rigid movement of the tongue depended on coordinates x and y, rather than just y. Moreover, the tongue's boundary the rigid body movement in x,y plane displacement was not driven by a function of lingual pressures, as Nicosia et al.in [42], but an imposed rigid body motion. The result was a dimensionless formulation for each of the regimes and it was solved numerically using a commercial Computational Fluid Dynamics (CFD) software known as COMSOL.

Finally, Nicosia et al. in [43] modeled the physics of food bolus containment, i.e. how bolus remains in the oral cavity by lingual gestures before its propulsion to the pharynx with the geometry in Figure **2-3**, and compared its behavior with different viscosities. To this end, the study used an explicit finite element hydrocode with a Lagrangian description, but due to large grid deformations, the solutions presented instabilities and numerical associated errors that terminated them prematurely, achieving only partial results. A more robust algorithm is needed for handling large displacements and deformations associated with this problem [43]. The results suggested that a more viscous bolus may reduce aspiration.

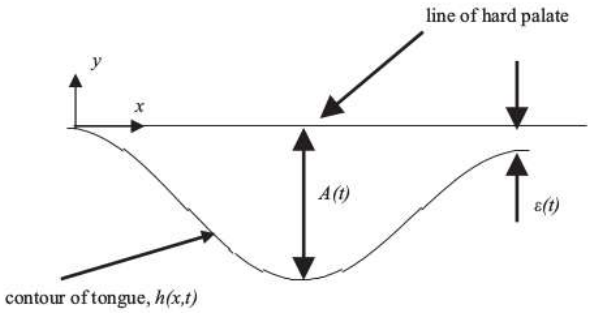

Figure 2-3: Model of bolus containment by [43]. Source: Taken from [43].

2.2.2 Pharyngeal stage

The models of pharyngeal transport consider a geometry between the Glossopalatal Junction (GPJ) and the UES, as were depicted in Figure **2-1**.

One to the first models was proposed by Chang et al. in [2] with a simplified axissymmetric geometry of the pharynx of variable radius and four nodal points displacements along the pharyngeal wall. The displacements were obtained from in-vivo studies from Cook et al. (1989) and Kahrilas et al. (1996)[23, 4]. Those in-vivo studies also gave closing times for

the GPL and UES, (0 s, 0.54 s) and (0.34 s, 0.104 s), respectively, which were also included in the model. As for the fluid studied, the model used a barium sulfate mixture with a density of $\rho = 1800kg/m^3$ and a viscosity of $\mu = 0.150Pa \cdot s$ that was assumed a single phase, incompressible and Newtonian, during the simulation. The modeling technique used Finite Element Method (FEM) to solve the partial differential equations and re-circulation zones were found for low viscosity fluids.

Later, Meng et al. in [37] further developed the geometry by Chang et al. in [2] exploring this time the transit of bolus with different rheological properties, see Figure **2-4**. The studied food boluses were water ($\rho = 1000kg \cdot m^{-3}$, $\mu = 0.001Pa \cdot s$), barium sulfate mixture ($\rho = 1800kg \cdot m^{-3}$, $\mu = 0.150Pa \cdot s$) and starch-thickened beverage (power law parameters $K = 2.0Pa \cdot S^n$, $n = 0.7$). Once again the solution was obtained with numerical methods, specifically a fully coupled Newton Raphson solution algorithm in conjunction with the Backward-Euler scheme with FIDAP [8]. In this work some of the boundary conditions were also modified, such as the normal stress on the GPJ, which were $1.6kPa$ for water and 20 for other fluids [37], as well as the opening and closing times of the GPJ. It was shown in this study that Newtonian and Power-law's fluids behave significantly different given the same boundary conditions. For instance, the flow rate and the shear rate would remain almost constant for the non-Newtonian fluid, while the Newtonian fluids showed marked changes.

On the other hand, Rosendall et al. in [49] simulated a more anatomically-accurate geometry extracted from video-fluoroscopic images. The simulation consisted of two states: a filling stage, where the bolus had a moving front, and then a moving boundary stage, where the bolus was propelled. However, the influence of the air and the muscles surrounding the pharynx were ignored. This work studied barium sulfate $\mu = 0.185Pa \cdot s$ and $\rho = 2840Kg/m^3$ and mixtures of Knott's strawberry syrup and E-Z-HD barium sulfate powder with $5Pa \cdot s$, $2360Kg/m^3$ and $45Pa \cdot s$, $2750Kg/m^3$. They found recirculation in some regions, for low viscosity fluids. However, their results, as with the previous studies, must be revised with caution since the computational capacity at the time obliged them to use coarse meshes.

2.2.3 Esophageal stage

The final stage considers the bolus' transit from the UES to the LES, which were shown in Figure **2-1**.

Misra et al. in [38] proposed a tubular geometry with finite length and deformable boundaries which would behave as a single wave governed by a power-law, representing in this manner the peristaltic transport, see Figure **2-5**. This model derived a dimensionless equation for pressure difference, and from that, the axial and radial velocity. Due to positive and

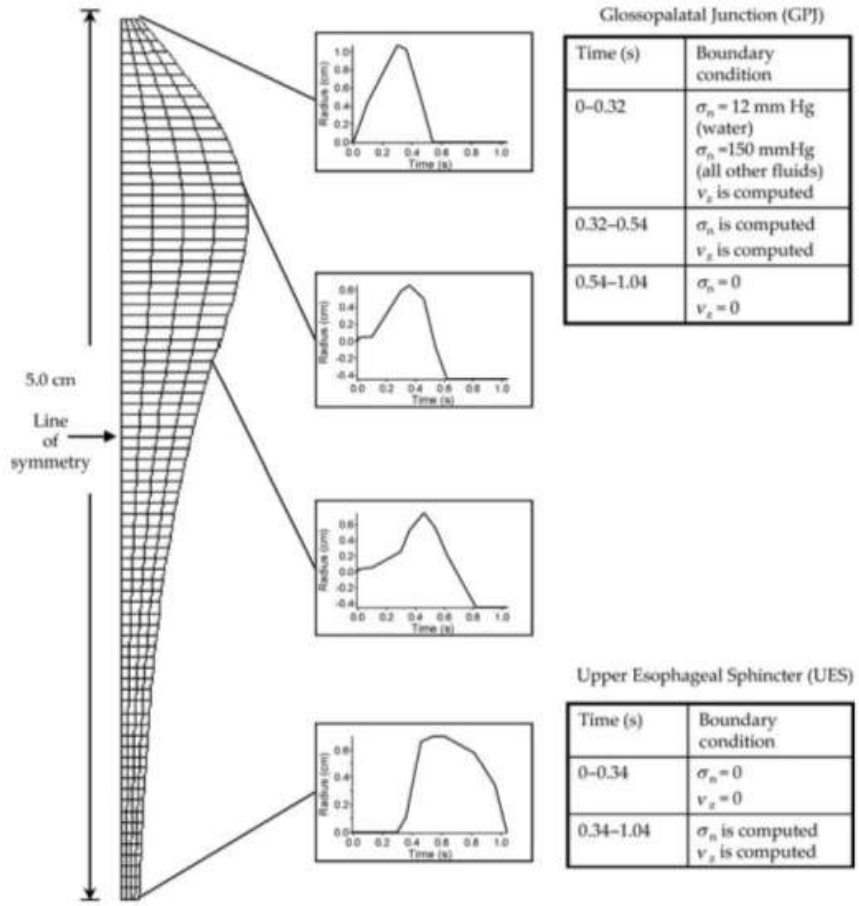

Figure 2-4: Three dimensional model by [37]. Source: Taken from [37].

negative pressure gradients originated from the moving boundary, the model predicted that the bolus had a forward motion within the wave and a retrograde motion beyond the wave, where the latter can be overcome with total occlusion of the esophagus, during single bolus transport. Moreover, shear stress analysis showed that pseudo-plastic fluid might be easier to swallow than a dilatant fluid.

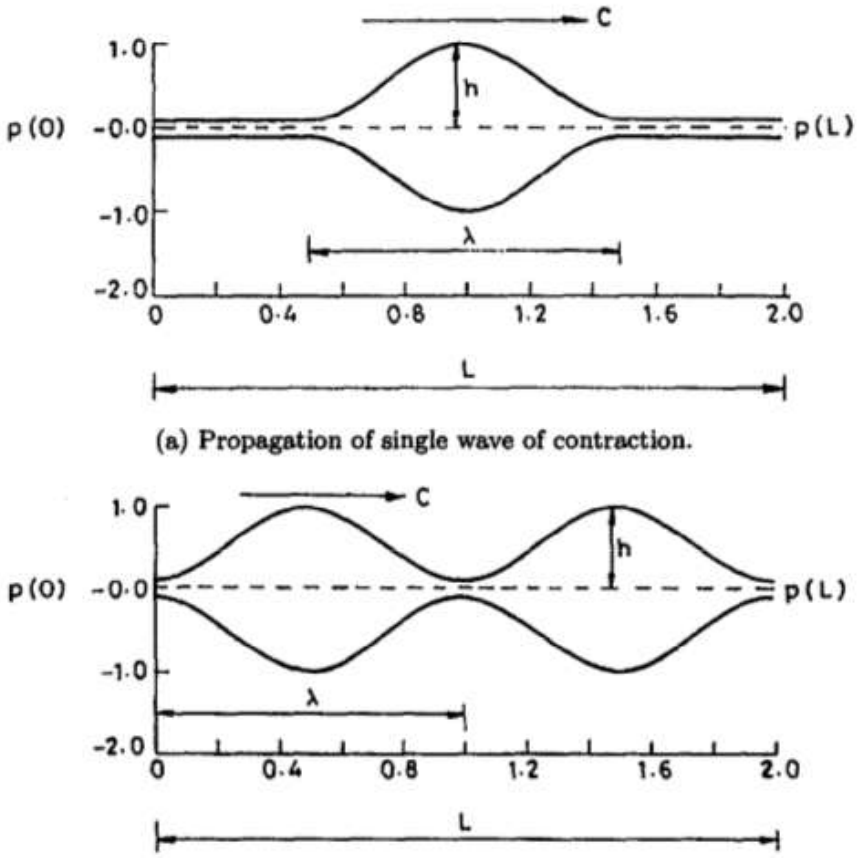

Figure 2-5: Model of peristaltic motion by [38]. Source: Taken from [38].

The next step was taken by Nicosia et al. in [45] who included the muscle mechanics of the esophageal wall, combining the contributions of active and passive components of circular muscle tension, as shown in Figure **2-6**. The esophagus was approximated as a thick-wall with two layers, distensible, axisymmetric and with an anisotropic fiber distribution. The model consisted of a relation between the transmural pressure difference and the circular muscle tension, a model of passive esophageal tension and an algorithm to combine the model equations with *in-vivo* data. Thus, the model described the relationship between longitudinal muscle tension and longitudinal muscle shortening, and the contribution of the collagen matrix surrounding muscle fibers to passive tension during normal and abnormal human esophageal bolus transport and in pathology scenarios.

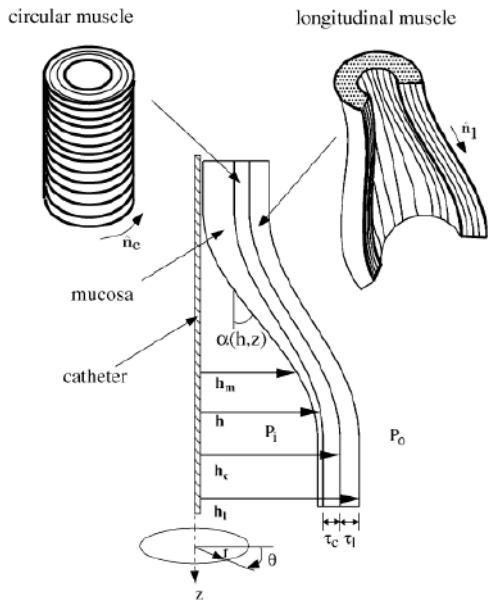

Figure 2-6: Model of peristaltic motion with muscle mechanics by [45]. Source: Taken from [45].

With a similar approach, Tripathi et al. in [55] studied the influence of viscosity during the esophageal stage and correlated its influence with local wall shear rate, pressure distribution, mechanical efficiency and trapping. For this, the model was solved numerically for a esophagus of finite length and considering free pumping, i.e. initial pressure difference is considered zero. The results were compared with manometric in-vivo studies from literature. A correlation between pressure and bolus viscosity was reported, suggesting that low viscosity is better for swallowing, since it requires less pressure to propel.

On the other hand, Kou et al. in [27] used a immersed boundary (IB) approach with discrete fiber-based, introduced in early bio-fluid structure interaction problems to simulate the peristaltic motion in [48]. In comparison to the previous works, the esophagus was modeled as a multilayer tube, including the effect of the mucosa layers and muscle activation, with different arrangements. They used as verification case the flow around a cylinder with different Reynolds number and compared the drag and lift coefficients, and the Strouhal number. The results were in good agreement with *in-vivo* bolus transport and would allow a correlation between data from manometry and ultrasound studies with the internal muscle activity.

A modified version of the IB model was presented by Kou et al. in [26]. It extended the fiber-based to a continuum mechanics-based model, using FEM, therefore (IB-FE). Furthermore, a new anisotropic adaptive interaction quadrature rule was introduced to deal with

Lagrangian-Eulerian interaction equation and the leakage issue when Lagrangian and fluid mesh became incompatible. This model allowed to handle non-linear elastic and fiber matrix interactions of the esophagus wall, making it more physiologically realistic. The model was compared with a 3D short tube, obtaining errors lower than 1% and maximum of 4%. One of the main conclusions was that spatially varying muscle fiber architecture approximate better to the luminal pressure pattern observed *in-vivo*.

An application of the previous model was made to evaluate several fibers architectures and its role in the peristaltic transition zone [26]. Additional to the findings from the previous models, it was determined that helical fiber architecture led to less circumferential wall stress during muscle contraction. On the other hand, the study pointed out that when analyzing the pressure *in-vivo* in distal and proximal segments of the esophagus, a big difference can be observed, and this behavior could not be explained by the dual-wave hypothesis, however, it may be attributed to non-uniform fiber structure.

2.2.4 Multiple stages

The previous models focused on a specific stage of swallowing, but there are some that take a broader approach and include several stages.

The three dimensional model by Mizunma et al. in [39] includes the oral propulsive and pharyngeal stages. The model assumed the bolus as a "jelly bolus", defined as a linear viscoelastic derived from the Maxwell three-element model. One of the highlights of this model was the emphasis given to the friction between the bolus and the organs, see Figure **2-7**. Using transient dynamics finite element formulation, the organs were modeled as linear elastic with values from literature, mainly solid elements, except for the epiglottis which was modeled with shell elements. Furthermore, stresses were prescribed in the tongue and the pharynx resulting in a feeding motion. On the other hand, some *in-vitro* tests were used to characterize the bolus' rheology and frictional coefficients. The results of this work can contribute to evaluate bolus' movement and coordination, and a validation with video-fluoroscopic results is desirable to refine the model.

Using a different technique, Ho et al. in [21] employed Smoothed Particle Hydrodynamics (SPH) to study the same region as the previous model. This approach would enable a 3D physiological realistic representation of the food bolus flow that include the nasal cavity, as shown in Figure **2-8**, and was validated comparing to the classical Hagen-Poiseuille flow in three dimensions, although the accuracy was depend on the particle's distribution. The swallowing simulation tested water ($\rho = 1000kg/m^3$, $\mu = 8x10^{-4}Pa \cdot s$) and honey-like bolus ($\rho = 1000kg/m^3$, $\mu = 10Pa \cdot s$). The oro-pharyngeal structures were modeled with the program Artisynth [52] with a mixture of rigid and elastic bodies, the latter modeled

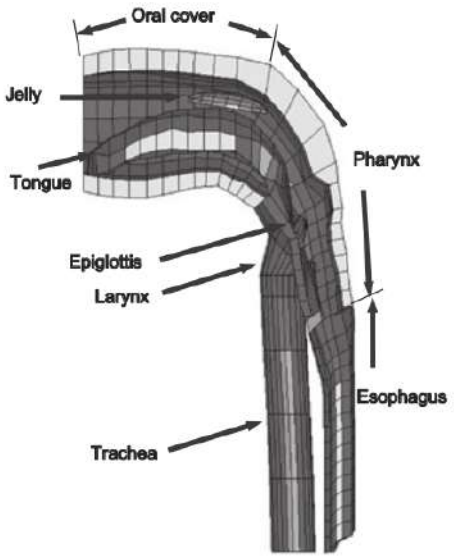

Figure 2-7: Three dimensional model of swallowing by [39]. Source: Taken from [39].

with FEM. It was found that the water bolus was most likely to enter the nasal cavity than was the honey-like bolus. The use of SPH presented however some challenges in regard to the boundary conditions. This work implemented a repulsive boundary condition, which prevented the particle entering the modeled tissue, but slip/no slip conditions can not be controlled and key parameters such as shear stress might have been overlooked.

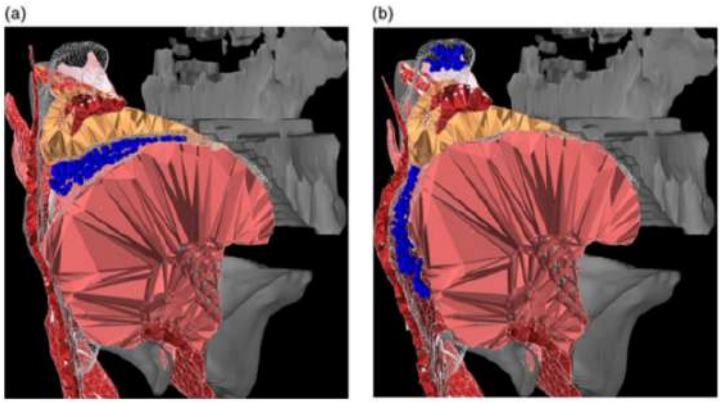

Figure 2-8: Three dimensional model of swallowing using SPH by [21]. Source: Taken from [21].

Additional to the previous model, Farazi et al. [11] also features the SPH technique to swallowing modeling, focusing on the application to clinical practice for visualization, training and diagnosis. This work also suggest the capabilities of inverse modeling capability of

Artisynth to approximate muscle activation.

2.3 In-vitro models of swallowing

Having a general idea of the different swallowing models, it was evident that most of them lack of some sort of validation. Therefore, this section describes some of the experimental arrangements, here called *in-vitro* studies, that represent processes typically found in swallowing and can serve as a basis to compare and construct future models.

There have been a large amount of studies on the theory of squeezing flow and its application to rheometry [9]. Even more so, the widespread of rheological test for food and food bolus. One of such techniques, the imperfect squeezing flow, was evaluated by Terpstra et al. in [53]. The geometry of the experimental bench is basically the geometry proposed by Nicosia et al. in [42], where two circular disks squeeze a fluid in between. The experimental test studied semisolid food products such as custard and mayonnaise, with different fat ratios, and arachid oil and treacle syrup. The results of flow index showed discrepancies with the lubricated and non-lubricated flow theory and is attributed to friction effects, pseudo-thixotropic behavior and buoyancy, as well as limitations in the measurement instruments, such as the elastic response and instrumental artifacts.

Another technique was proposed by Loubens et al. in [6], which studied the pharyngeal peristalsis and its application to flavour release with a lubrication analysis. The setup consisted of two hydrophobic cylinders and a device to deposit a thin film of fluid, representing saliva. The aim of this work was to analyze the fluid mechanics of pharyngeal peristalsis and to develop a simple biomechanical model in order to understand the role of saliva an bolus viscosity on the coating of pharyngeal mucosa. Moreover, a mathematical model based on the lubrication theory for Newtonian liquids was developed in dimensionless form. One of the limitations of the model was the rigidity of the cylinders that represent the mucosa, but this was later addressed in an extended dimensionless model that took into account the mucosa deformability [5]. The thickness of mixed food bolus and saliva predicted by the latter study was approximately 20 μm, which was 3 μm thicker than the previous one.

Finally, a notable experimental setup, known as the Cambridge Throat, was developed by Mackley et al. in [32], which represented the bolus propulsion during the oral stage. The setup was a modified rheometer with a simplified 2D geometry of the oral cavity and a constant torque cam system. Such a system represents the tongue when dragging the food bolus through a soft tube, as depicted in Figure **2-10**. This setup tested fluids encountered in dysphagia treatments such as thickeners as “Nautilis Resource ThickenUp” and “Xanthan gum”. Hayoun et al. in [18] further evaluated the Cambridge Throat with a deeper parametric study to understand the oral phase of swallowing of Newtonian liquids. It aimed

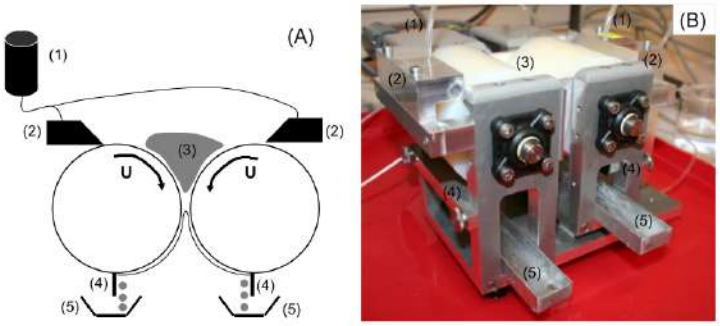

Figure 2-9: Experimental bench of pharyngeal peristalsis simulator. (1) saliva food, (2) slot coater, (3) food bolus, (4) scraper, (5) collector. Source: [6].

to describe how the flow rate was affected by viscosity and volume of food bolus, and also the effect of the gap between the swallowing force and the gap between the palate and the tongue-like cam.

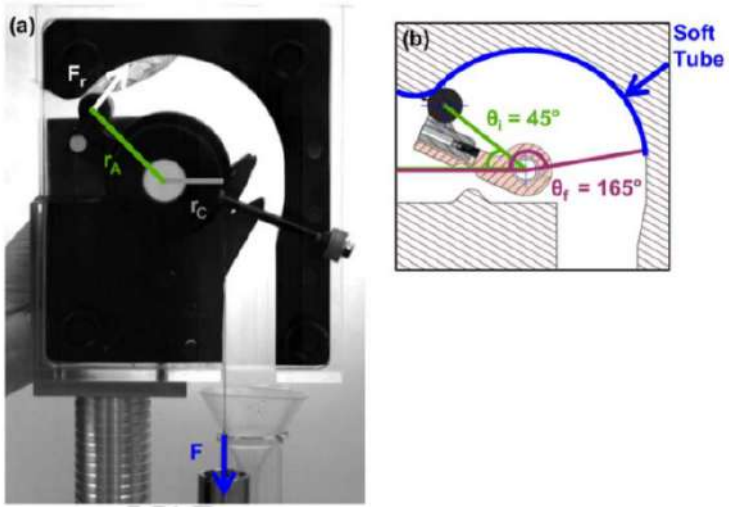

Figure 2-10: Experimental bench of bolus propulsion using a cam system by [32]. (a) Overview of the experimental setup. (b) detailed drawing of the arm and roller without liquid. Source: Taken from [32].

Proposed *in-silico* physiological accurate model of oral-swallowing

Contents

3.1 Materials and methods

The *in-silico* modeling of oral-swallowing began with the construction of the physiological accurate geometry of a healthy adult, capturing the sagittal movement of the tongue's dorsum from real time magnetic resonance imaging (RT-MRI) procedure. This movement was taken as driven boundary of the fluid flow, but the cloud of points from the RT-MRI had to be first interpolated in time and space before introducing them in the commercial Computer

Fluid Dynamics (CFD) program, ANSYS FLUENT. The initial mesh was constructed with the interpolated profile at time zero and User Defined Functions controlled the displacement of the tongue.

The desired output variables from the model were the flow rate and velocity of the fluid at the tongue's outlet, see Figure **3-1.c.** , and the force and shear stress over the tongue. Their behaviors were depended on time, the rheological properties (density and viscosity) of the fluid under consideration and how long the event lasted (event time), which constituted the factors. In order to analyze the influence of every factor, a second order Box-Behnken's design was used, since the model suggested non-linearity in pilot simulations. This incomplete three-level factorial surface response design is commonly used when there are three or more factors and it was chosen over a central compose design since only three levels were evaluated.

However, the analysis up until now can only correlate relations and the incidence of individual factors on the effects of the phenomena. But do not address conjugate effects of the factors, which by experience of fluid mechanics must certainly occur, i.e. the combined effect of viscosity, density and velocity. Therefore, the input factors were grouped together Reynolds numbers, and the effects were grouped into force and friction coefficients.

3.1.1 Geometry and Displacement Functions of the Tongue

Using RT-MRI is possible to visualize the transit of the food bolus through the oral cavity *in-vivo* and non-intrusively. To construct the geometry of the physiological accurate model, images from a healthy adult were used to extract the tongue's motion in the sagittal plane. The images and contours of the biological structures of the oral cavity were provided by Mathieu Labrunie, Pierre Badin (GIPSA-lab,Grenoble, France) and Laurent Lamalle (IRMaGe, Grenoble, France), which used supervised machine learning techniques to identify the contours for each frame [29], as shown in Figure **3-1**.

During the oral phase of swallowing, the movement of tongue's *dorsum* involves accommodation and propulsion of food bolus. Considering the total tongue's *dorsum* proved to be difficult to implement in CFD since accommodation movement introduced noise to the simulation. Therefore, it was decided to select portion of the total tongue's *dorsum*, an "Active Tongue Region" (ATR) as the moving boundary wall (in red), which participated more "actively" in the propelling of the food bolus. However, no anatomical reference in tongue's *dorsum* could be establish to select the ATR and it should be revised with caution.

On the other hand, the curve described by the ATR at the final time frame, when making full contact with the palate, was selected to be the palate's fix wall boundary. Notice that the latter is a simplification, since the palate also moves in the oral phase. Finally, the

posterior wall of the schematic in Figure **3-1.c.** represents the outlet of the food bolus and the beginning of the pharynx. These walls correspond to the boundary conditions that will be described in detail in Section 3.1.3.

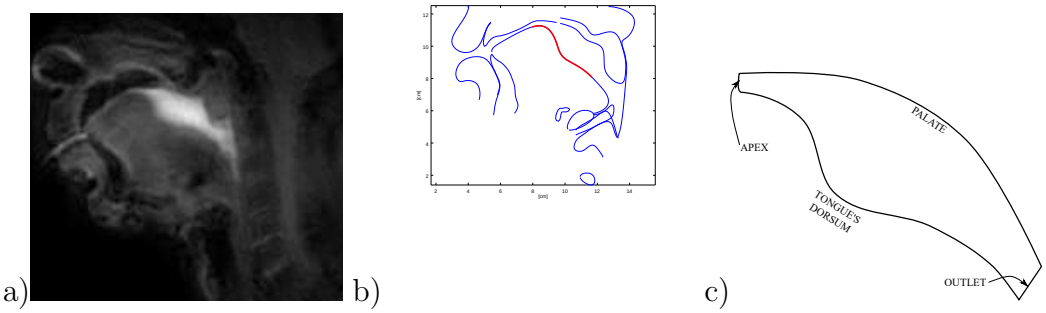

Figure 3-1: a) Original frame from the RT-MRI. b) Extracted contours of the structures in the oral cavity extracted from the RT-MRI (blue) and the ATR contour (red). c) Geometry of the physiological accurate model of oral phase of swallowing.

After processing the data from the RT-MRI frames, a discrete tongue's contour in form of a point cloud was obtained for each time step. However, this discretization do not necessarily coincide with the temporal and spatial discretization used during simulation, since they depend on the mesh's parameters and time step definition. Therefore, a 6th order polynomial approximation using Least Square Method (LSM) was performed in time and space to interpolate the data from the RT-MRI. By doing so, one can assign the position of any point at any given instant in time, even if it does not coincide with the original discretization from the image processing technique.

The function $\overline{\mathbf{X}}_{tongue}(x, y, t)$ is defined by a matrix of coefficients, see Equation 3.1.1, and is used as motion boundary condition in flow field solution for the domain in Figure **3-1.c**.

$$\overline{\mathbf{X}}_{tongue}(x, y, t) = \begin{pmatrix} \sum_{i=1}^{N} a_i(t) x^i \\ \sum_{i=1}^{M} b_j(t) y^i \end{pmatrix} \tag{3-1}$$

Where the spatial coefficients $a_i(t) = \sum_{k=1}^{P} c_k t^k$ and $b_j(t) = \sum_{l=1}^{Q} d_l t^l$ are function of the temporal coefficients c_k and d_l. Finally, the polynomial order was held the same, N = M = P = Q = 6, for X and Y, and both, spatial and temporal discretization. Additionally, k, l, i, j are index counters.

3.1.2 Assumptions and constrains

From a physical and mathematical point of view, one can analyze swallowing as a transient fluid structure interaction problem, with both fluid dynamics and nonlinear elasticity. From the elasticity perspective, each biological structure in the oropharyngeal tract would consist in general of soft tissue with anisotropic, nonlinear-elastic and non-homogeneous properties, which experience large deformations [14]. On the other side, from a rheological perspective, the food bolus can be non-linear, semi-solid, viscoelastic fluid, whose properties may depend on temperature, time and shear-rate [43, 2].

In the oral phase of swallowing, the food bolus is transported to the pharynx by a squeezing motion of the tongue. In this sense, it is a marching unsteady fluid flow problem that evolves due to the effect of a boundary motion (tongue) over the fluid domain. The fluid domain is represented in the Figure **3-2**, taken at the mid-sagittal plane.

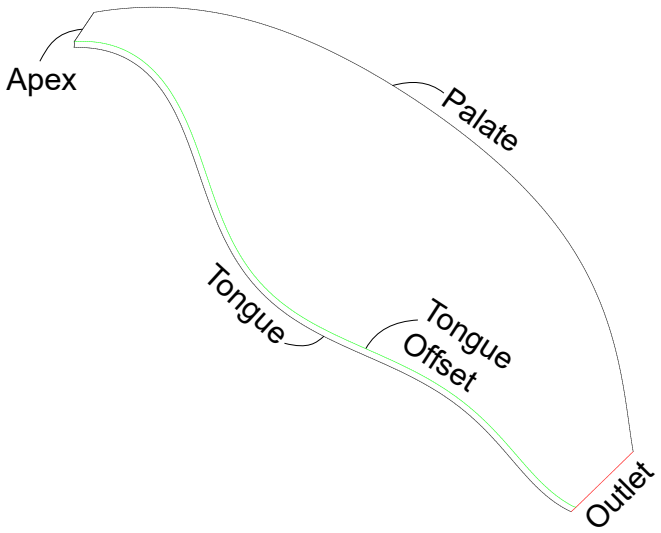

Figure 3-2: Detail on the fluid domain of the oral cavity with the main boundaries. Notice that there is an artificial tongue's offset, which was necessary to guarantee fixed cell height in the vicinity of the tongue's *dorsum*. Source: Author.

The present work considers the following assumptions and simplifications:

The food bolus is assumed Newtonian fluid with homogeneous rheology, (density and viscosity). In order to have a first approximation of the order of magnitud of the Reynolds numbers, it is considered a rectangular tube with the flow conditions of the food bouls in the oral cavity, from rough estimations on bolus' velocity and geometry were taken from

literature. Nishikubo et al. in [46] estimate a bolus velocity during swallowing pressure of approximately 0.107 m/s, meanwhile Burbidge et al. in [28] estimate a peak velocity during propulsion of 0.4 m/s. Additionally, the gap between the tongue and the palate changes during the swallowing event, from around 0.03 m to zero. As result, an approximate Reynolds number would be $Re \approx 1000 - 4000$, for water. Therefore, a flow between the laminar and transit regime is expected.

Fluid dynamics of food bolus' flow is modeled as a two dimensional mid-sagittal flow, which is a major simplification according to [13, 25, 31] who demonstrated strong three dimensional behavior in the food bolus's flow. It was however implemented due to lacking data on three dimensional tongue movement. The flow is also assumed single-phased, ignoring the influence of air in the oral cavity, since it is also assumed that the food bolus' filled the oral cavity completely.

The deformation of the tongue's *dorsum* due to the interaction with the fluid (hence the fluid structure interaction) is assumed negligible in comparison to the deformations inherent to the *dorsum*'s motion.

Finally, this work considers exclusively the oral phase of swallowing, in which the tongue plays a major roll as it propels the food bolus to the pharynx. However, an artificial gap between the tongue and the palate was assumed due to limitations in numerical solutions to resolve contact interaction between meshes.

3.1.3 Governing equations

The Newtonian, homogeneous, single phase food bolus is governed by the continuity Equation 3-2 and conservation of momentum equation, see Equation 3-3.

$$\nabla \cdot \mathbf{u} = 0 \tag{3-2}$$

$$\rho \left(\frac{\partial \mathbf{u}}{\partial t} + \mathbf{u} \cdot \nabla \mathbf{u} \right) = -\nabla P + \mu \nabla^2 + S_\phi \mathbf{u} \tag{3-3}$$

These equations represent three scalar equations, where $\mathbf{u} = [u, v, w]^T$, is the velocity field. u, v, w are the velocity components in x, y, z, P is the pressure field, S_ϕ are the sources, here represented by the body forces due to gravity, and ρ and μ are the density and dynamic viscosity of the fluid, respectively.

The problem states the following boundary conditions, Equation 3-4.

$$\begin{aligned} \mathbf{u}(\mathbf{X}_{tongue}, t) &= \frac{d\mathbf{X}(x,y,t)_{tongue}}{dt} \\ \mathbf{u}(\mathbf{X}_{hardpalate}, t) &= 0 \\ P(\mathbf{X}_{outlet}, t) &= P_{ref} \\ \mathbf{u}(\mathbf{X}_{apex}, t) &= 0 \end{aligned} \tag{3-4}$$

Where $\mathbf{X}(x, y, z, t)$ corresponds to the spatial coordinates of every given point inside the fluid domain at any given time and $\mathbf{u}(\mathbf{X}_{tongue}, t)$ corresponds to the resulting velocity field of the fluid adjacent to the tongue's boundary.

The boundary of the tongue is also subjected to the constrains of non penetrating and no slip condition. This condition is a simplification of the food bolus flow as demonstrated by [44], since it does not take into account the effect of the mucosa over the tongue's *dorsum*.

Finally, the initial conditions considered are presented in Equations 3-5,3-7 and 3-6.

$$\mathbf{u}(x, y, z, 0) = 0 \tag{3-5}$$

$$\mathbf{X}_{palate}(x, y, z, 0) - \mathbf{X}_{tongue}(x, y, z, 0) = H_0 \tag{3-6}$$

$$\mathbf{u}_{tongue}(x, y, z, 0) = 0 \tag{3-7}$$

The Equation 3-5 corresponds to the initialization of the velocity field, and Equations 3-6 and 3-7 describe the tongue's initial position and velocity at beginning of the oral propulsion stage.

3.1.4 Simulation setup

Simulations were carried out in ANSYS Fluent® that is based on the classical CFD, see Appendix A.1. The parameters for all simulations include fluid flow in instantaneous Navier-Stokes regime, semi-implicit method for pressure-linked equations, SIMPLE, for pressure-velocity coupling, first order upwind for advection discretization/interpolation term and a first order implicit backward Euler for transient discretization. Convergence absolute criteria for residuals was set to 1×10^{-4} for continuity and velocities.

According to the Courant-Friedrichs-Lewy condition (CFL), [20], the parameters of the simulation Δt, $\mathbf{u}$ and Δx, gave a Courant number of 0.01 which satisfied the CFL condition, allegedly due to small time step ($0.0008s$) used during simulations, where this fine temporal discritezation was necessary due to dynamic meshing algorithms.

The ATR's movement was controlled by a User Defined Function (UDF), see Appendix B, by imposing the position of each node on the tongue's boundary for every time step according to $\mathbf{X_{tongue}}(x, y, t)$. The UDF used "Define Grid Motion", receiving as input the matrices of coefficients that govern the polynomial that define the tongue's contour. The development of this algorithm was inspired by a document by Madhawa Hettiarachchi, in which a UDF imposed movements to the brain contour using an oscillatory function [1]. As a result of the tongue's boundary movement, the fluid domain changes and the mesh had to be adjusted, therefore, it was necessary to implement the dynamic mesh algorithms such as Laplacian-Smoothing and Remeshing, see Appendix A.2. The parameters to set up the dynamic mesh were found by trial and error, and depended on the spatial and time discretization of the problem. The Table **3-1** lists the parameters used for this case.

Table 3-1: Modified parameters of the dynamic mesh algorithms used for the simulations. The rest of the parameters were left with default values. They depend heavily on the mesh and time step size.

Smoothing	
Type	Laplace
Laplace node relaxation	0.5
Convergence tolerance	0.001
Elements	All
Remeshing	
Minimum length scale (mm)	0.04
Maximum length scale (mm)	0.03
Maximum cell skewness	0.7

Figure **3-3** presents peaks of continuity residuals at fixed time steps, which were independent of the mesh and the simulation parameters (initialization, time step, pressure-velocity coupler). The origin of the first peaks were attributed to flow establishment, but the next peaks were attributed to discontinuities in flow rate when calculated from the change of volume, $Q_{calc} = \Delta V/dt$, as can be see in Figure **3-4**. These discontinuities were inherited from the tongue's *dorsum* movement, which is governed by the function Equation 3.1.1. At these specific time steps, the change of tongue's *dorsum* motion was so small (near to zero) or so large, that the change in volume resulted in a discontinuity.

However, since the number of iterations were sufficient to achieve the convergence criteria of

[1] See: https://goo.gl/2kXxVa

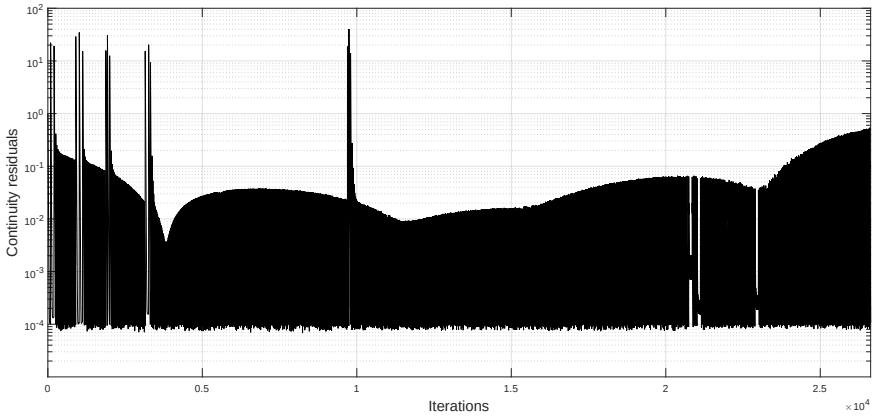

Figure 3-3: Continuity residuals for a domain with water ($\rho = 998.2kg/m^3$ and $\mu = 0.001003kg/m \cdot s$). In every loop of iterations the continuity is satisfied with a criteria of 10E-4, however there are four visible peaks at the beginning of the iterations. Those peaks were independent of the fluid under consideration and the time deglutition event.

10^{-4} at every time step, thus it did not diverge numerically, we proceeded to the design of experiments for the simulations. Future works must smooth the change in tongue's *dorsum* motion to avoid these peaks.

3.1.5 Design of experiments

The computational model itself is not enough to describe the oral phase of swallowing, since it did not show the influence of rheology parameters and the velocity of the tongue on the output parameters, such as the expulsion velocity, the fluid pressure and the shear stress over the tongue. To this end, a full factorial statistical analysis was used to evaluate the influence of such variables in the model under consideration, specifically a 3^3 with three factors and three levels for each. The input factors are the bolus' rheology, that is density and viscosity, and the duration of the swallowing event, i.e. the event time. The Table **3-2** shows the proposed levels for each factor. Notice that the extreme values for bolus' rheology are the properties of water and glycerin, and on the other hand, the extreme values for event time were taken as the time of the video-fluoroscopic swallowing study (0.72s) and half this value.

Such a scheme gives a total of 27 simulations named after the levels in Table **3-2**. For example, the simulation **e012** is the simulation with an event time: $0.72[s]$ (Level 0), a bolus with density: $1129[kg/m^3]$ (Level 1), and viscosity: $0.799[kg/m - s]$ (Level 2).

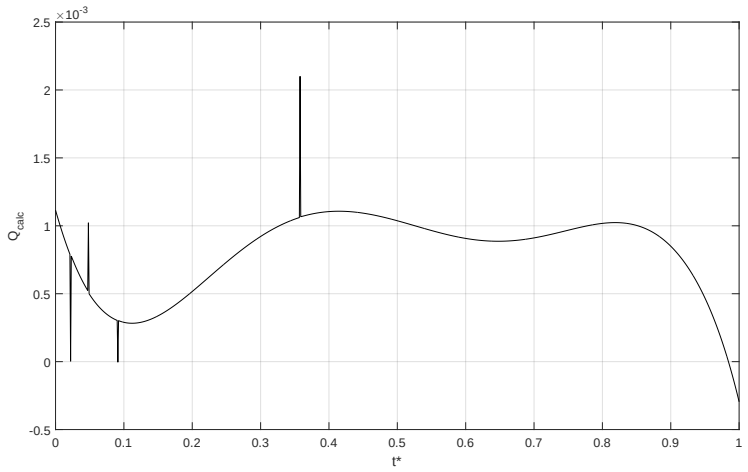

Figure 3-4: Calculated flow rate from the volume of the fluid domain against non dimensional time.

Table 3-2: Values for each level of each input variable.

Level	**0**	**1**	**2**	**units**
A. Event time	0.72	0.54	0.36	s
B. Density	998.2	1129.05	1259.9	kg/m^3
C. Viscosity	0.001003	0.4000015	0.799	$kg/m-s$

From the model, it was expected to understand the behavior in time and the incidence of the input factors in several field variables, ϕ_i. The following Table **3-3** list the mathematical definition for each. Notice that these values are per unit dept (in meters) since it is a two dimensional model.

3.1.6 Construction of the dimensionless model

In the problem at hand, the loads over the tongue can be described as, $f(t_e, \nu, \rho, L_e) = 0$, where L_e is a characteristic length. Following the Buckingham π theorem, this meaningful function can be rewritten in terms of dimensionless parameters constructed from the original variables. The proposed dimensionless parameters for this work were Reynolds number, Force and Friction coefficients, i.e. $\mathcal{F}(Re, C_f, C_\tau) = 0$. Tables **3-4 -3-5** describe how the coefficients were constructed, where $A_t^{000}(t_0)$ is the tongue's area of the simulation $e000$ at a time $t = 0$, A_s cross-sectional area, and P_w is the wet perimeter. The latter was an analogy to the wet perimeter to calculate the hydraulic length. The temporal mean values of the field variables, F_{tongue} and τ_t, were used, see Table **3-3**.

Table 3-3: Mathematical description of monitors during simulation.

Name	**Report Type**	**Field variable**	**Description**
A_t	Sum	Face area magnitude	$\sum_{i=1}^{n} \phi_i$
Q_{out}	Volume flow rate	-	$\sum_{i=1}^{n} \vec{v_i} \cdot \vec{A}_i$
v_{outlet}	Area-Weighted Average	Velocity magnitude	$\frac{1}{A} \sum_{i=1}^{n} \phi_i \lvert A_i \rvert$
F_t	Integral	Static pressure	$\sum_{i=1}^{n} \phi_i \lvert A_i \rvert$
τ_t	Integral	Wall shear stress	$\sum_{i=1}^{n} \phi_i \lvert A_i \rvert$

Table 3-4: Reference parameters for the dimensionless model.

Name	Symbol	Definition
Ref. Time	t^*	t/t_e
Ref. Area	A_t^*	$\frac{1}{2}(max(A_t^{000}) + min(A_t^{000}))$
Ref. Length	L_e	$\frac{(A_s(t_{end}) - A_s(t_0))}{mean(P_w(t_{end}) + 2 \cdot A_s(t_{end}), P_w(t_0) + 2 \cdot A_s(t_0))}$
Ref. Vel.	V_e	L_e/t_e

Table 3-5: Definition of the dimensionless parameters as a function of the characteristic variables.

Name	Symbol	Definition
Reynolds number	Re	$\frac{V_e L_e \rho}{\mu}$
Force coefficient	C_f	$\frac{F}{1/2 \rho V_e^2 A_t^*}$
Shear coefficient	C_τ	$\frac{F_\tau}{1/2 \rho V_e^2 A_t^*}$

3.2 Results and Discussion

3.2.1 Polynomial fitting of tongue's contour

The functional $\overline{\mathbf{X}}_{\mathbf{tongue}}(x, y, t)$ that resulted from the double polynomial approximation was compared to the raw points cloud from RT-MRI data. The relative error between their L^2-norm is depicted as box plots in Fig. **3-5** for each time frame. The box plot contains the mean, first and third quartile, confidence interval for the mean (1.5 times the interquartile range (IQR)), values between one to three times IQR ('+') and values over three times IQR ('o'). After trial and error, a sixth order polynomial approximation was selected since it presented an error below 1% for every discrete point and time frame without comprising calculation's time.

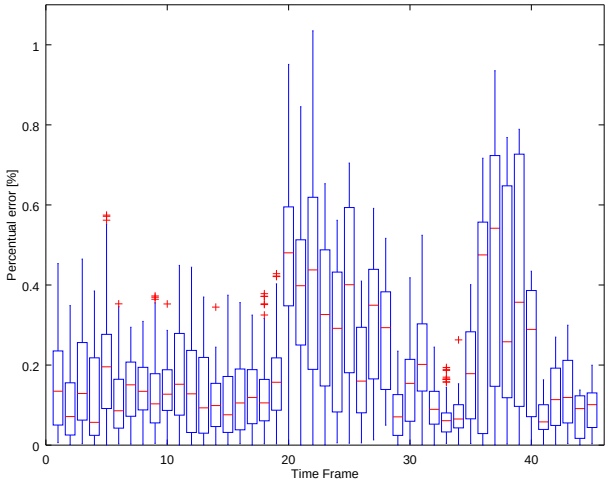

Figure 3-5: Box plots for each time frame comparing the measurements of RT-MRI and the sixth order double polynomial approximation.

3.2.2 Mesh's convergence test

The mesh consisted of quadrilaterals elements in the vicinity of the moving boundary and triangular elements in the interior of the domain, see Figure **3-6**. This hybrid mesh was necessary to have a good resolution of the shear stress and to guarantee the stability of the dynamic mesh algorithm. An additional UDF between the interface of quadrilaterals and triangular elements was compiled to control the displacement of the offset boundary. Furthermore, the dynamics mesh algorithms were Smoothing in the region of quadrilaterals and Smoothing and Remeshing in the region of triangular elements.

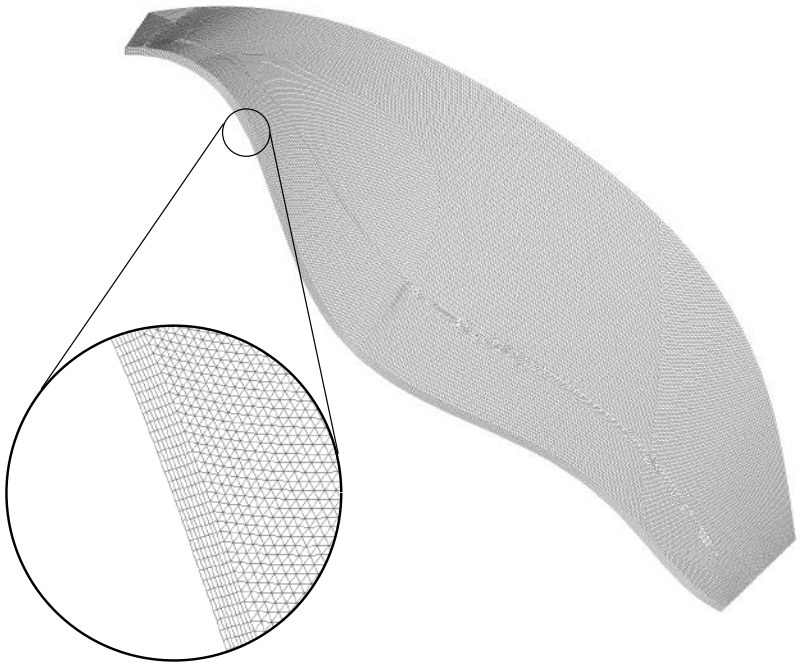

Figure 3-6: Final mesh with 53900 elements and a detail on the interface between quadrilateral and triangular mesh.

Convergence test was performed considering as reference the case $e000$, where the tongue's shear force was computed for each time step. As it can be seen in the Figure **3-7.a**, at the instantaneous level, there is no significant variation of the shear forces over the tongue, as a function of the number of elements. However, when analyzing the mean temporal shear force in Figure **3-7.b**, it convergence to a mesh of 53,900 elements. The latter was used in all the following simulations.
Finally, it was expected that this model was sensible to continuity errors since its domain was in general deformed, re-meshed in time, and had a single outlet and on inputs. However, when comparing the flow rate, computed as the difference in volume in one time step, versus the flow rate value in every time step, $\int v_{outlet} dA_{outlet}$, the relative error was not greater than 4% before the time step 960. After that time step, the relative error began to grow abruptly and the it returned to values below 2%. Such behavior was due to the beginning of backflow at the outlet, which obeyed to physiological movements of the patient's tongue.

3.2.3 Behavior of oral propulsion as a function of time

The figure **3-8** shows the change in ATR, A_t, along the dimensionless time, $t*$. As expected, the behavior was the same for all the simulations, since the displacements were controlled by the UDF. Notice additionally that this behavior was independent from the event time, which evidences that t_e is an adequate parameter to describe the phenomena. The tongue's area per unit width oscillates around $568 \pm 4.76 \times 10^{-4} [m^2/m]$, which is a variation below 0.83%. Inflection points in the curve indicate changes from contraction to elongation of tongue's area, and the tongue's area presented a constant elongation after $t* = 0.5$.

In the upper region of Figure **3-8**, one can find the evolution the tongue's boundary for five specific time steps. As expected, the tongue moves upward, decreases the oral cavity's volume and squeezes the bolus against the palate, and therefore propels it outward. However, close inspection to the RT-MRI demonstrates that regions of the ATR contracts while other regions expands, simultaneously. During most of the event, the net effect of contraction and expansion results in a decrease in the oral cavity volume, but this net change in volume was turned positive approximately at the time step 960, experimenting an expansion and therefore leading to a back flow as demonstrated by the continuity error presented before.
On the other hand, Figure **3-9** shows the flow rate at the outlet, Q_{outlet}, represented by three clearly defined curves. The curves corresponded to the event times, t_e, and therefore, each one contained nine experiments. The differences in the flow rates are consistent with continuity assumption, where the displaced volume by the tongue is the same as the volume flowing out. Where the latter is independent of the fluid properties. The Figure **3-9** shows to the wight and zoom in section, where the three curves intersect in zero and then turns negative. In practice, this represents that approximately at $t* = 0.9845$ the mean flowrate at the outlet started to be predominantly backflow. However, this does not necessarily means

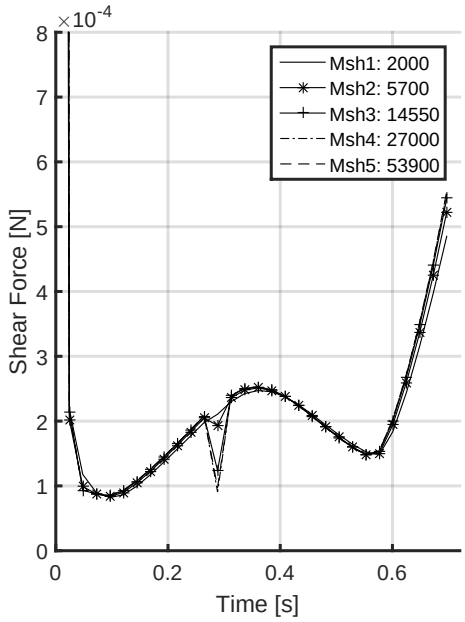

a)

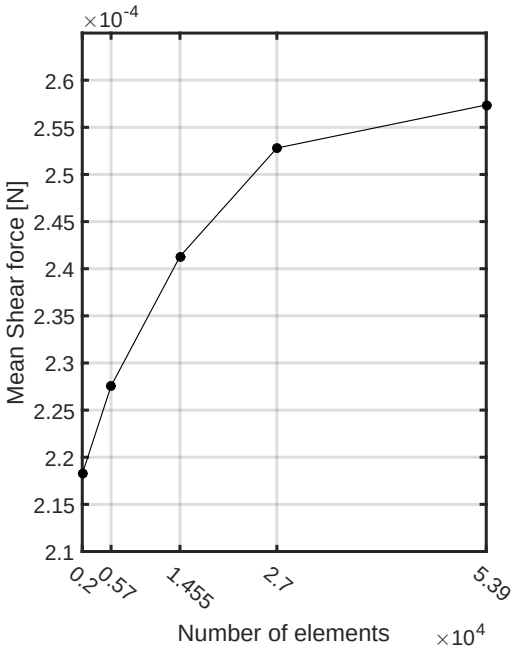

b)

Figure 3-7: Convergence test for different meshes. a) Evolution in time of the shear force integrated over the tongue for each mesh, and b) Temporal mean shear force as a function of the number of elements for each mesh.

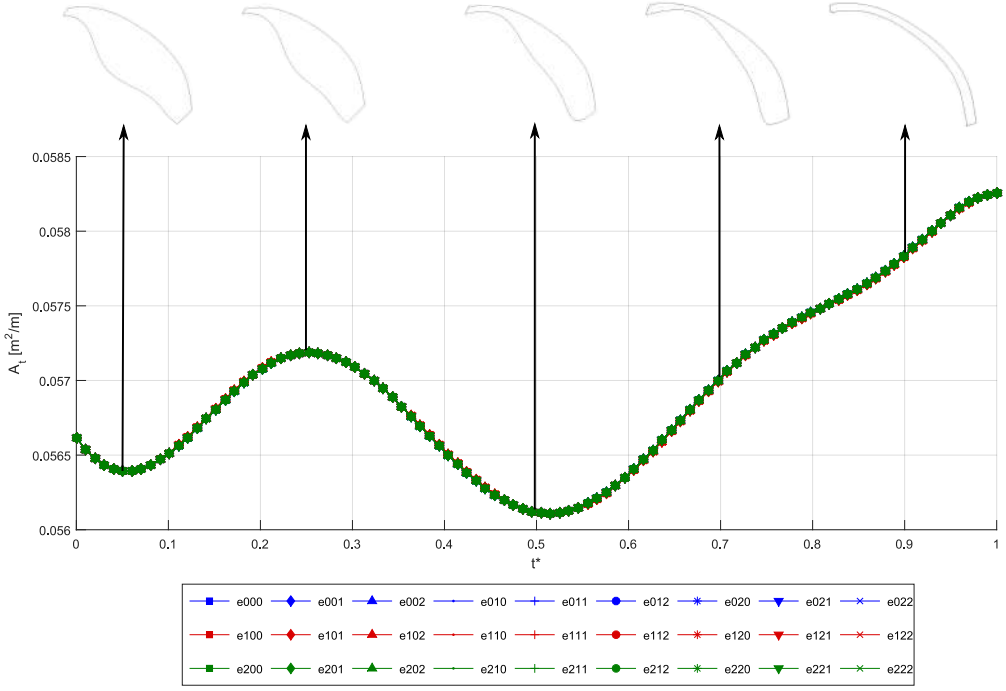

Figure 3-8: Temporal evolution of ATR's area per unit meter of depth for each experiment.

that no backflow was presented before this time as would be discussed when presented the pressure force over tongue.

As expected, the magnitude of the flow rate was bigger for a shorter event time, i.e. faster swallowing, but the amplitude' differences were bigger for a shorter time events. Consequently, this models predicts lower mean flow rate and lower fluctuations for people with slower swallowing. Additionally, the peak of flow rate is experienced at the middle of the event. For this patient, the calculated temporal mean flow rates were $8.42 \times 10^{-4}[m^3/s/m]$, $11.23 \times 10^{-4}[m^3/s/m]$,$16.85 \times 10^{-4}[m^3/s/m]$ for t_e of $0.8s$, $0.6s$ and $0.4s$, respectively.

The flow rates' peaks at the beginning were attributed to the instantaneous acceleration of the tongue as the equations tries to fulfill the boundary conditions.

The temporal evolution of the velocity at the outlet, v_{outlet}, in Figure **3-10**, is close related to the flwo rate. Once again, there are three curves that corresponded to the event times, where a bigger velocity magnitude corresponded to shorter event times. In this case, the velocity presented an increasing behavior twice, that ended at $t* = 0.4$ and $t* = 0.9$, and rapidly decay towards the end of the simulation. Similarly to the flow rate, such behavior obeys exclusively to the UDF that control the displacement, and in consequence obey to swallowing habits of the patient.

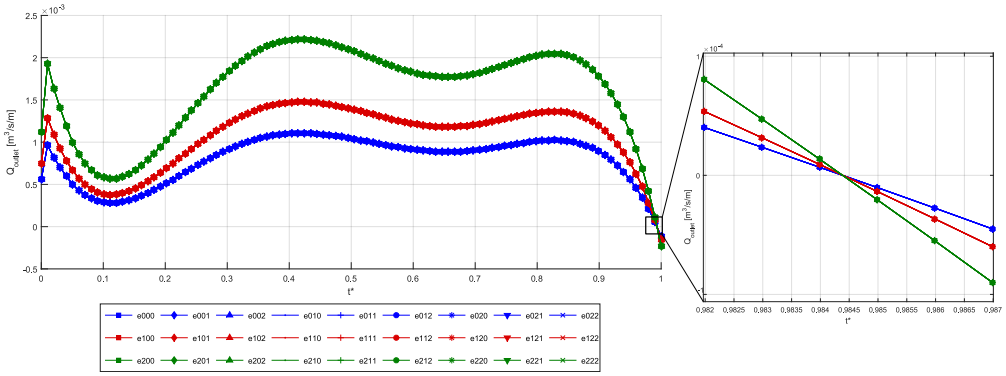

Figure 3-9: Temporal evolution of the outlet flow rate for each experiment.

In contrast to the flow rate, the velocity presented variations between simulations with the same event time, which is not consistent with the previous results in Figure **3-9**, since the difference between those should be an scalar factor of the tongue's outlet area. The fluctuations cannot be explain in tongue's outlet area variation between simulations, since it deformed and re-meshed consistently in all of them. Therefore, it is suspected that numerical vices in regard of quantity calculation may be affecting the result, especifically, that velocity is not calculated with the scalar product with the area while flow rate is. The values for mean temporal velocity at the outlet were $0.1234[m/s/m]$ $0.1646[m/s/m]$ $0.2425[m/s/m]$, corresponding to the event times 0.8s, 0.6s and 0.4s.

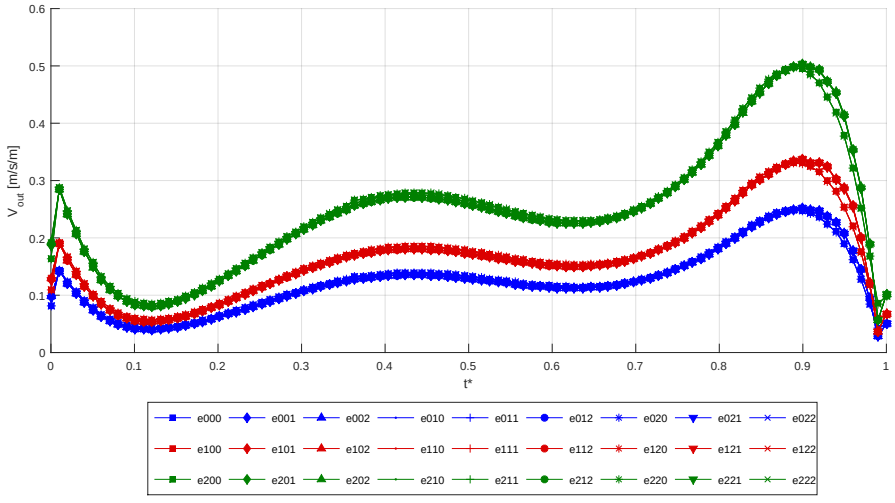

Figure 3-10: Temporal evolution of the outlet velocity for each experiment.

Finally, the Figures **3-11** and **3-13** show the semi-logarithmic pressure force, F_t, and shear force, F_τ, over the ATR as a function of the dimensionless time. In contrast to the previous field variables, all input variables had an effect on the output.

On one hand, F_t in Figure **3-11** depicts two groups of experiments: The one with larger forces corresponds to 18 experiments with levels 1 and 2 of viscosity, and the other group of 9 experiments with level 0 of viscosity. The experiments are further divided according to the event time and density, where the event time has a larger influence on the velocity than the density. The Figure **3-11** also depicts images of the evolution of the pressure contours at certain time steps for the simulation e222.

The Figure **3-11** also shows two blank spaces in the first 100 time steps and towards the end for nine simulations, due to small negative forces on the tongue surface. These negative forces are attributed to local back flow at the boundary of the tongue, which was evident due to the local mesh refinement in the vicinity of the tongue. Such a behavior was consistent for all fluids with viscosity $\mu = 0.001003kg/m - s$, whose dynamics are expected to be in the transition regime.

The simulations with viscosity levels 1 and 2 presented a peak at the beginning of the event that corresponded to the initial acceleration of the tongue, as was also evident in the velocity at the outlet.

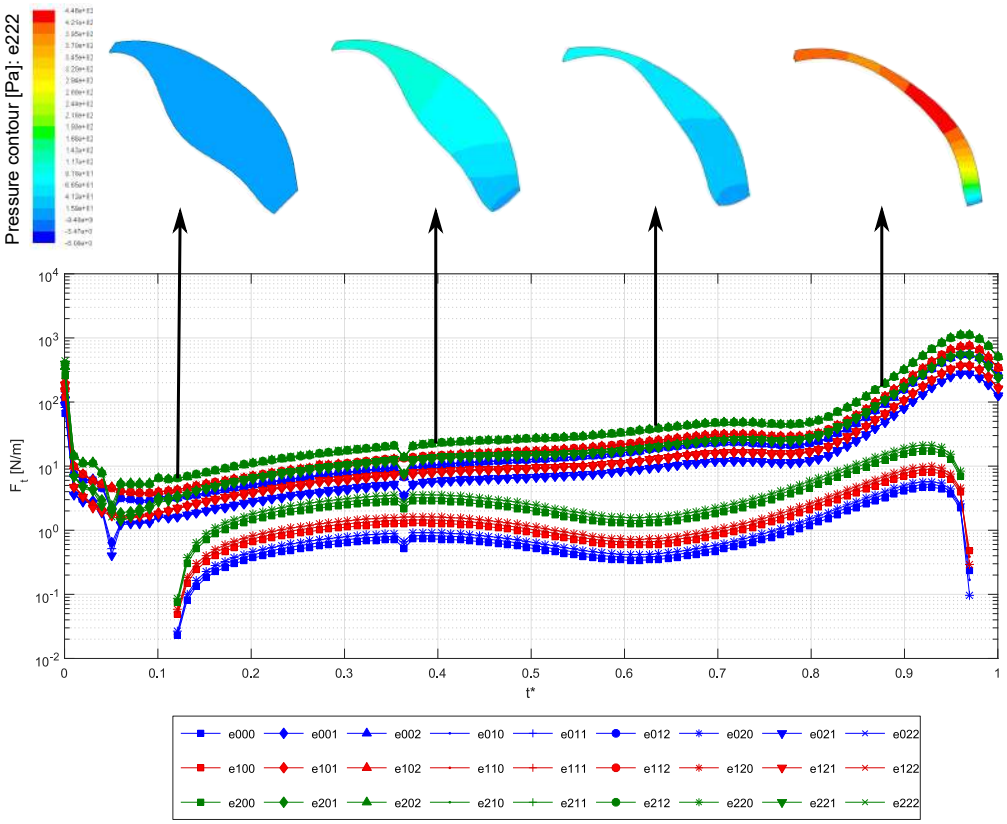

Figure 3-11: Temporal evolution of the force over the ATR for each experiment.

On the other hand, Figure **3-13** shows F_τ as a function of the dimensionless time. Similarly to force behavior, it also has an logarithmic behavior and the stratification of the experiments depended on viscosity, event time and density, exactly in the same way as the previous case. The scale, however, is one order of magnitude smaller than the force over the tongue.

From these results, it can be stated that larger viscosity and faster swallowing would lead to greater pressure force and shear force over the tongue. Notice additionally that the force and shear force had a very similar behavior, but the contribution to the total force for the experiment, $F_{total} = norm(F_t, F_{tau}$ see Figure **3-12** for simulation $e000$, was mainly due to the pressure force, with the exception of the beginning and the end of the swallowing event. The Figure **3-12** zooms in the last time steps of the event, where the net pressure force decay to zero and continued to be negative at approximately the dimensionless time $t* = 0.94$.

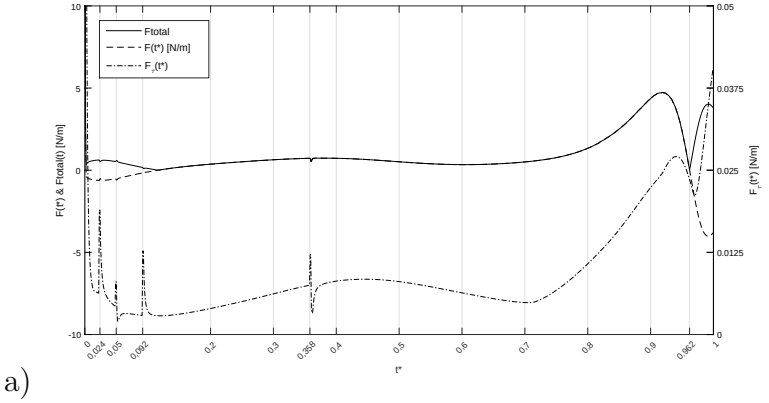

a)

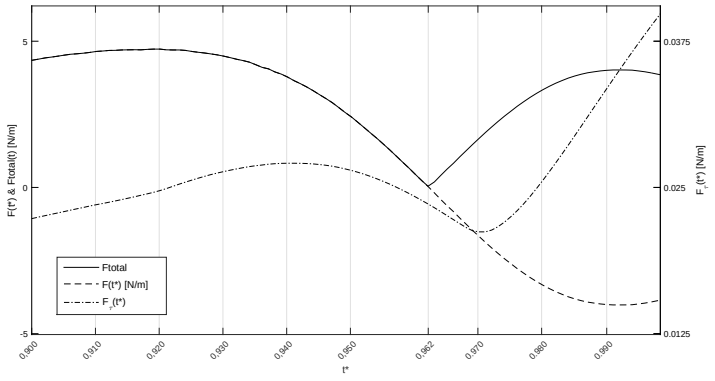

b)

Figure 3-12: a)Comparison of force, shear force and total force as a function of dimensionless time. b) Detail on the forces towards the end of the simulation where back flow was found.

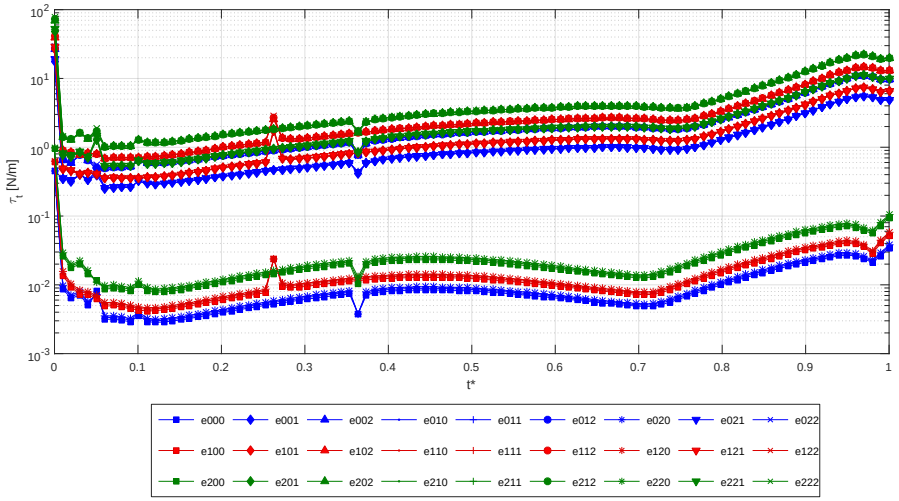

Figure 3-13: Temporal evolution of the shear force over the ATR for each experiment.

3.2.4 Box-Behnken's design

The previous section illustrated qualitative correlations among the variables as a function of the time steps. However, the quantitative influence of each factor and the interaction between factors was not described. For this reason, it was necessary to resort to statistical methods, specifically, a 3-Factor Box-Behnken as the surface response design to quantitative analyze the data.

The experiments (in this case simulations) for Box Behnken design can be represented in a cube plot as in Figure **3-14** and is a quadratic design. Notice that such a design do not use the simulations at the corners of the cube.

Following the terminology of design of experiments (DOE), the input variables are now called the factors or main effects, and the obtained field variables after simulations, are the responses. These responses are taken as the average values in time, $\frac{1}{\Delta t}\int_{t_0}^{t_{end}} \phi(t)dt$.

As before, each factor has three levels (0,1,2) but this time they would receive the values -1, 0, 1 and are denoted as coded units. To analyze the overall behavior of the variables, mean quantities for the responses are used and summarized in Table **3-6**.

Each response can be written as a function of the main effects, their interactions and their quadratic terms, see Equation 3-8

$$\hat{y} = \mu + \beta_0 x_0 + \beta_1 x_1 + \beta_2 x_2 + \beta_{01} x_0 x_1 + \beta_{02} x_0 x_2 + \beta_{12} x_1 x_2 + \beta_{00} x_0^2 + \beta_{11} x_1^2 + \beta_{22} x_2^2 \qquad (3\text{-}8)$$

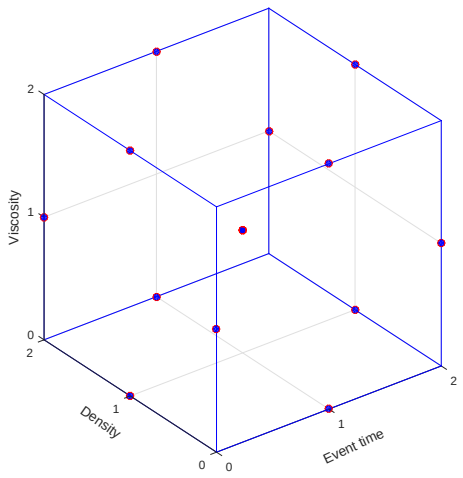

Figure 3-14: Graphical representation of the surface response design known as Box-Behnken.

Table 3-6: Summary of simulations and temporal-averaged results. Here the factors A, B, C correspond to event time, density, and viscosity, respectively.

A	B	C	$\overline{Q_{out}}$	$\overline{v_{outlet}}$	$\overline{F_t}$	$\overline{\tau_t}$
1	0	1	0.0017	0.2422	36.5074	3.3927
1	-1	0	0.0017	0.2423	20.9211	1.7218
0	0	0	0.0011	0.1616	13.4465	1.1424
0	0	0	0.0011	0.1616	13.4465	1.1424
0	1	-1	0.0011	0.1649	1.4411	0.0122
1	0	-1	0.0017	0.2476	2.7943	0.0208
1	1	0	0.0017	0.2425	21.7344	1.7406
0	-1	-1	0.0011	0.1648	1.1586	0.011
0	0	0	0.0011	0.1616	13.4465	1.1424
-1	-1	0	0.0008	0.1211	8.5249	0.8472
-1	0	1	0.0008	0.121	15.2642	1.6791
-1	0	-1	0.0008	0.1236	0.7298	0.0077
0	-1	1	0.0011	0.1615	25.0715	2.2528
-1	1	0	0.0008	0.1211	9.4958	0.8511
0	1	1	0.0011	0.1615	25.4422	2.2587

Where μ corresponds to the overall mean, β_i with i = 0,1,2 are the adjusting coefficients for the main effects, β_{ij} with i,j = 0,1,2 are the adjusting coefficients for the interactions and β_{ii} with i,i = 0,1,2 are the coefficients for the quadratic terms.

$$\begin{pmatrix} \overline{Q_{out}} \\ \overline{v_{outlet}} \\ \overline{F_t} \\ \overline{\tau_t} \end{pmatrix} = \begin{pmatrix} 0.0010 & 0.00045 & 0 & 0 & 0 & 0 & 0 & 0 & 0 & 0 \\ 0.1616 & 0.061 & 0 & 0.002 & 0.0203 & 0 & 0.002 & 0 & 0 & 0 \\ 13.447 & 5.993 & 0.304 & 12.020 & 1.134 & 0.588 & -0.757 & 0 & 4.795 & 0 \\ 1.142 & 0.436 & 0 & 1.192 & 0.145 & 0 & -0.012 & 0 & 0.425 & 0 \end{pmatrix} \begin{pmatrix} 1 \\ A \\ B \\ C \\ AA \\ BB \\ CC \\ AB \\ AC \\ BC \end{pmatrix} \quad (3\text{-}9)$$

The Equation 3-8 shows several things. On one hand, the model for $\overline{Q_v}$, states that the mean flow rate depends exclusively on the event time. On the other hand, the model of $\overline{v_{outlet}}$ shows a dependency of event time, viscosity and a contribution from the quadratic term of event time.

On the other side, $\overline{F_t}$ and $\overline{\tau_t}$ depends on event time and viscosity, quadratic effects and interactions of between the main effects. The density seems to play a minor role in both cases.

3.2.5 Dimensionless model

With the definition of the dimensionless parameters in Table **3-5**, Force and Shear force coefficients as a function of Reynolds number are shown in Figures **3-15** and **3-16**. Both functions fitted a logarithmic decay following the Equation 3-10 and the coefficients listed in Table **3-7**, within a 95% confidence bounds.

Additional to the 3^3 experiments used for the factorial design, nine more simulations were made since there was a gap of two order of magnitudes between the Reynolds numbers. These new experiments used a viscosity of $\mu = 0.017kg/m-s$ which gave Reynolds numbers between 10^0 to 10^1.

$$f_i = a_i \cdot Re^{b_i} + c_i \cdot Re^{d_i} \tag{3-10}$$

Table 3-7: Coefficients for the exponential functions in Figures **3-15** and **3-16**. The values in parenthesis correspond to the 95% confidence bounds.

Function i	a	b	c	d
1	10,730	-2.314	4029	-0.1586
	(10,710, 10,740)	(-2.315, -2.313)	(4004, 4055)	(-0.1629, -0.1544)
2	7094	-2.313	2496	-0.1752
	(7083, 7105)	(-2.314, -2.312)	(2478, 2514)	(-0.1807, -0.1698)
3	5368	-2.312	2030	-0.1694
	(5360, 5376)	(-2.313, -2.311)	(2015, 2044)	(-0.1753, -0.1634)
4	427.9	-2.372	157.1	-1.013
	(409.6, 446.1)	(-2.394, -2.35)	(136.4, 177.7)	(-1.103, -0.9223)
5	298.1	-2.343	94.42	-0.9459
	(291.9, 304.2)	(-2.353, -2.333)	(87.18, 101.7)	(-1.006, -0.8858)
6	227.9	-2.334	63.99	-0.8968
	(224.9, 230.9)	(-2.34, -2.328)	(60.31, 67.67)	(-0.9472, -0.8463)

The exponential fitting was made with Nonlinear Least Squares method and the algorithm Trust Region. The goodness of fit was tested by calculating the square of the correlation between the response values and the predicted response values, R-square. A value of 1 was obtained for all the functions.

For Reynolds of order 10^2, the coefficients of friction were almost constant, therefore this model predicts that shear force over the tongue was independent of rheological parameters, and to a similar degree, the same also applied to the force coefficients.

On the other hand, when analyzing the results for a given fluid, the force coefficients presented a consistent quadratic behavior while the shear force coefficient a linear behavior as a function of Reynolds number. Therefore, the model predicts a force and shear force over the tongue as a unique function of event time, for the same fluid. However, since these curves

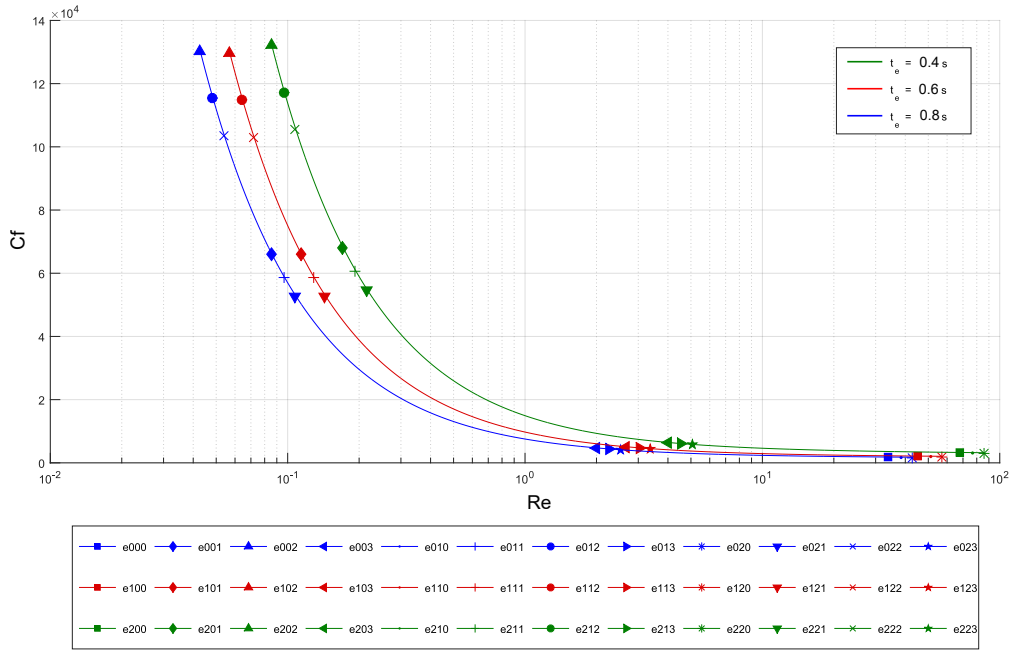

Figure 3-15: Coefficient of force as a function of Reynolds number.

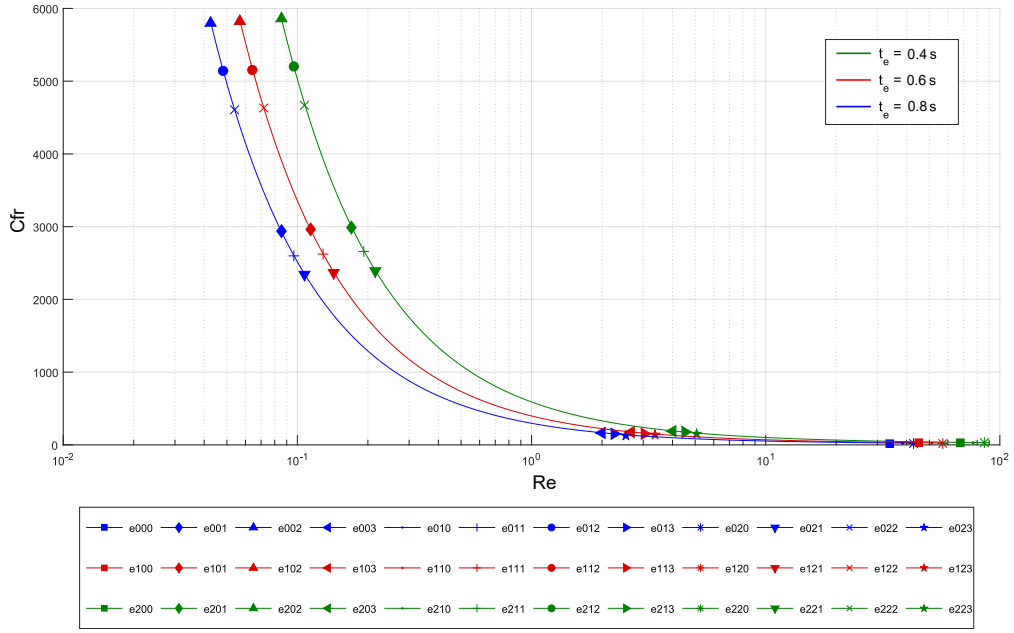

Figure 3-16: Coefficient of friction as a function of Reynolds numbre.

for each fluid were constructed with only three points, more data points are necessary to see if this relation holds for all other event times.

3.2.6 Validation of the dimensionless model

In order to give a first validation to the proposed dimensionless model, a 28th simulation is set up with the same parameters and mesh as the ones used in Section 3.1.4. This time however, the factors to be evaluated are: time event of $0.72[s]$, viscosity of $0.02[kg/m-s]$ and density of $1000[kg/m^3]$.

Following Table **3-5**, the new simulation has a Reynolds number of $Re = 1.634$ and coefficients $C_f = 968.12$ and $C_{fr} = 42.238$. On the other hand, Equation 3-10 predicts the force and friction coefficients are predicted to be 953.26 and 44.93, respectively. A comparison results in percentage errors of 1.53 % and 1.64% for force and friction coefficients, respectively.

Since the mesh and solution parameters for the commercial software were left unchanged, the differences can be attributed to truncation and approximation errors of the solution algorithms.

Validation approaches

Contents

This chapter presents some approaches to validate the *in-silico* model from the previous chapter. The first approach compares the velocity of the centroid of the food bolus during oral swallowing of a healthy adult with the outlet velocity of the simulation. The second approach compares forces over the tongue and the flow rate at the outlet with two additional simpler *in-silico* models. Finally, a novel experimental bench of oral swallowing with a linearized geometry is presented, from which velocity fields were extracted using PIV measurements. The velocity fields are compared with simulations in CFD, in which the contour extraction methodology was the same as in the previous chapter.

4.1 *In-vivo* food bolus mean velocity

The first approach compares the velocity of the food bolus' centroid with the mean outlet velocity of the simulation. Since we are comparing particle motion with fluid dynamics, the conclusions are restricted to indirect comparisons.

On one hand, the procedure to determine the food bolus' centroid velocity using MATLAB ®is as follows: the images in DICOM format were transformed to binary images with the algorithm *im2bw(Image,level)* [1], with a threshold level of 0.7. This enabled to increase the contrast of the food bolus; the remaining uneven dark regions inside the food bolus were eliminated with the algorithm *imfill(BW,'holes')* based on morphological reconstruction [51][2]. Next, the contour of a completely filled shape was identified using the algorithm *bwlabel* [17] [3] and finally the centroid was extracted using the algorithm *regionprops(BW,'centroid')* [4]. The complete code can be found in Appendix D.

However, such a method was prone to false positives, since additional closed contours were identified due to bright zones not corresponding to the food bolus. To identify which ones corresponded to the food bolus and which were fake, the algorithm also calculated the distance between centroids of consecutive frames and a threshold was given; when this distance surpassed the threshold, that centroid was considered as noise and was discarded.

The Figure **4-1** shows the processed images for a time t_0, where the red circle is the location of the centroid for that specific instant. This procedure was repeated for a total of 38 frames. Note that the selected time span used for the bolus' centroid tracking was the same as the one used for tongue's *dorsum* contour in the simulation, 0.72 s.

With the location, $\mathbf{X_{centroid}}$, of the centroid for every frame and the time between frames, $dt = 0.019[s]$, the mean velocity calculated as $\mathbf{v_{centroid}} = \Delta\mathbf{X_{centroid}}/dt$.

On the other hand, a simulation was set up with the same boundary, initial and geometric conditions as the model in the previous chapter, but with a major change in the fluid. Barium sulfate mixture is commonly used as contrast fluid in a videofluoroscopic tests and is a well known shear-thinning (pseudoplastic) non-Newtonian fluid, that is depended on the ratio of sulfate barium dissolved in water and the temperature. This fluid can be characterized as a 250% w/v barium sulfate mixture with a density of $\rho = 1800kg/m^3$, and a Power Law model's parameters of $K = 2.0Pa \cdot s$ and $n = 0.7$ [2].

[1] See https://la.mathworks.com/help/images/ref/im2bw.html
[2] See:https://la.mathworks.com/help/images/ref/imfill.html
[3] See: https://la.mathworks.com/help/images/ref/bwlabel.html
[4] See: https://la.mathworks.com/help/images/ref/regionprops.html

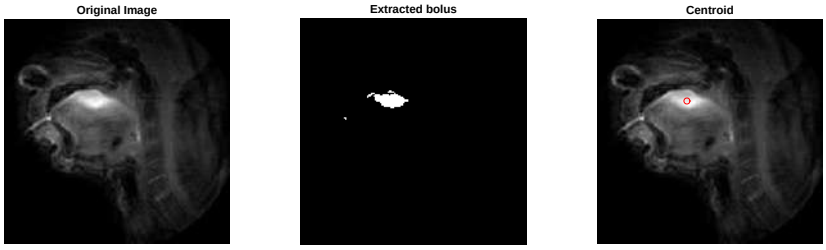

Figure 4-1: Tracking of the centroid of the food bolus from a dynamic magnetic resonance of a healthy young adult (21-35) using barium sulfate mixture as contrast agent.

The mean velocities obtained for the food bolus' centroid in RT-MRI and the mean velocities during simulations were plotted against dimensionless time in Figure **4-2**. The null hypothesis states that there is no significant difference between these two set of data, called populations, and the difference observed can be attributed to sampling or experimental error. And in order to test this null hypothesis, we used a non-parametric (distribution free) tool called Chi Square test for independence [36], with 38 degrees of freedom, corresponding to the number of frames (39) minus 1. The value of the test was $\chi^2 = 547.9$, which is higher than the critical Chi Square value for 38 degrees of freedom ($\chi_c^2 = 58.384$ for a confidence level of 95%), therefore the null hypothesis was rejected, and these populations are statistically different.

This result might obey to several reasons: First, we were not comparing the same variables, bolus' centroid velocity versus mean fluid flow velocity; Secondly, 39 frames in 0.72s seems to be a small temporal resolution and the tracked centroid had several accelerations which make difficult to compare directly between time frames of the image and the simulation. Finally, the resolution of the RT-MRI [224x224 px] images might have been insufficient to correctly define the bolus' contour.

Despite the differences, both distributions showed equivalent orders of magnitudes as can be seen when comparing the distributions in box plots as in Figure **4-3**.

4.2 Comparison with simpler models

Additionally to the physiological-accurate model presented in Chapter 3, two simpler geometries of squeezing fluid flow were also analyzed with the same methodology to serve as reference. One corresponds to two horizontal cylindrical plates with translational rigid body motion and the other to a wedge-like geometry with a rotatory rigid body motion, as shown

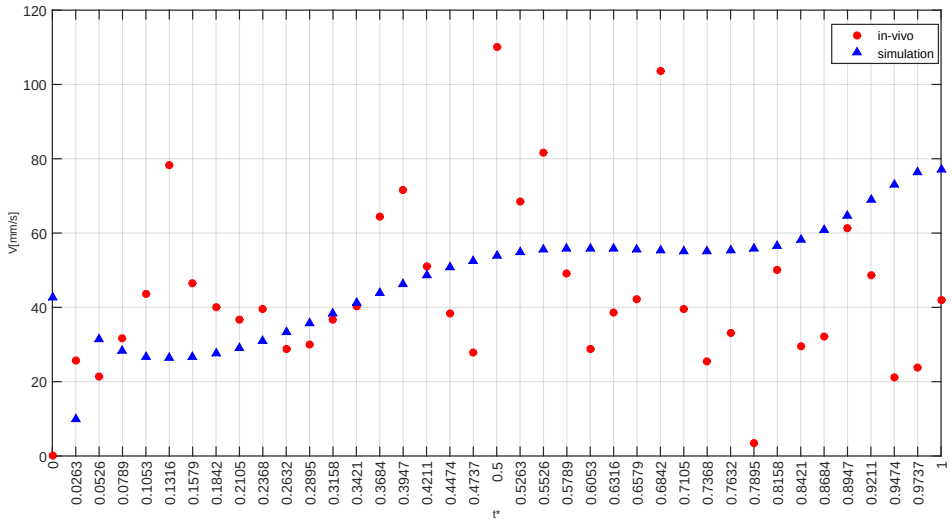

Figure 4-2: Mean velocities distributions in time against the dimensionless time, for the food bolus' centroid in RT-MRI and the mean outlet velocities during simulations.

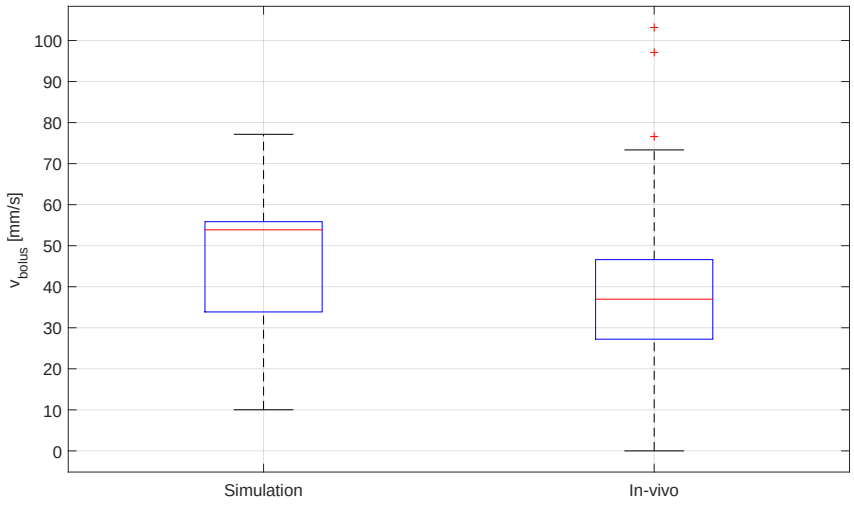

Figure 4-3: Box plots comparing the velocity distribution between the bolus' centroid velocity during the *in-vivo* test and the mean velocity magnitude during the simulation.

in Fig. **4-4**. In these geometries, the tongue is represented by the moving plate, the hard palate by the stationary plate, and the fluid to-be-squeezed between them represents the food bolus. These models were named model 1 and model 2, respectively, while the previous physiological accurate model was named model 3. A dimensionless formulation for model 1 was initially proposed by Weinbaum et al. [50] as a rheological case of squeezing flow and later used by Nicosia et al. [42] in the context of swallowing.

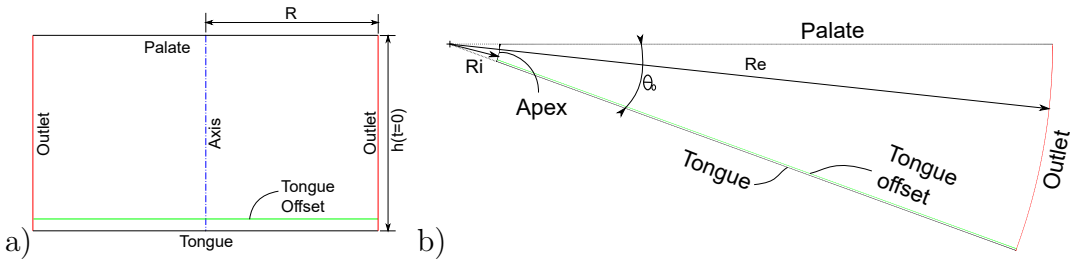

Figure 4-4: Simplified models of bolus propulsion a) two-plates model (Model 1) and b) wedge-like model (Model 2). Where, R = 20 mm, h(0)=20 mm, R_i=5mm, R_e=65.5 mm, $\Theta_0 = 20^o$

In order to make these models comparable to one another, the change in volume of model 3 and the duration of the event (event time) were taken as reference. Therefore, the geometry and dynamics of the other two models must comply to the same restrictions. However, notice that model 1 has axial symmetry while model 2 and 3 have planar symmetry hence their results are per unit meter of depth. Therefore, the latter models were multiplied by a scale factor of 30 mm (approximately the mean value of the tongue width [42]), to make them comparable to the results of model 1. This constant was also used to scale the results of flow rate, force and shear force over the tongue, which are reported later on in this section.

The change in volume for model 3 was $\Delta V = 18.18mL$ (for scale reference a teaspoon has 5 mL) with a duration of 0.72 s. Hence, the volume of models 1 and 2 must change similarly, within the same amount of time. These values were obtained using the parameters shown in Figure **4-4** achieving changes in volume for model 1 and 2 of $\Delta V = 18.08mL$ and $\Delta V = 18.09mL$, respectively.

Notice in Figure **4-4** that Model 2 has an extra wall in the upper left corner with no-slip and non-penetrability conditions. This extra wall corresponded to an artificial gap between the tongue and the hard palate that does not exist during normal swallowing, but due to increased complexity in the numerical model, the contact physics between the tongue and the hard palate was ignored.

4.2.1 Mesh and moving boundary considerations for simpler models

In contrast to model 3, the geometries of models 1 and 2 used layering exclusively for the dynamic mesh algorithm. Therefore, the simulation of the simpler models did not involve remeshing. Their meshes were made of quadrilaterals-only and had a static zone in the vicinity of tongue-boundary, that did not change its thickness as the tongue-boundary moved. Additionally, they had an inflation with smooth transition with a grow rate of 1.2, as can be seen in Figure **4-5**.

As before, an absolute criteria for continuity residuals was set to 1×10^{-4} and a mesh convergence was tested using shear force integrated over the tongue's surface, as can be seen in Figure **4-6**. The selected meshes had 18,000 elements for model 1 and 70,400 elements for model 2, with a refinement in the vicinity of the tongue's boundary as can be seen in Figure **4-5**. Since the model had a moving boundary, special attention was given to the properties in this boundary and therefore, an integral property such as shear stress was selected for the convergence test. However, future works should address methodologies to evaluate convergence of dynamic meshes.

All models follow the formulation in Section 3.1, but with geometry and tongue dynamics. That is, the function that defines the movement of the tongue, $h(\mathbf{X}_{tongue}, t)$, and the initial geometry, H_0. For model 1 in Fig. **4-4**.a. $h(\mathbf{X}_{tongue}, t) = v_{cte}$ with a director vector $\hat{n} = (0, 1, 0)$ and for model 2 in Fig. **4-4**.b. $h(\mathbf{X}_{tongue}, t) = \omega_{cte}$ with a director vector $\hat{n} = (0, 0, 1)$.

4.2.2 Comparison between *in-silico* models of oral swallowing

Average pressure, shear force over the tongue's surface and flow rate at outlet were computed at every time step., as shown in the semi-logarithmic plot in Figure **4-7** for water ($\rho = 998.2[kg/m^3]$, $\mu = 0.001003[kg/ms]$). On one hand, models 2 and 3 presented increasing behaviors with comparable magnitudes for both force and shear force, and on the other hand, model 1 also showed an increasing behavior but its force and shear force values were respectively 100 and 10 times smaller, when compared to the other models. The latter is probably due to the large difference in geometry of model 1 since it is essentially a radial flow.

Table **4-1** shows a summary of time integrals of the values shown Figure **4-7**. Specifically, for the mean pressure force $\bar{F}$, the mean shear force $\bar{S_f}$, and the mean volume $\bar{V}$, see Equations 4-1. Model 2 and 3 report comparable magnitudes in both force and shear force. Additionally, notice that the outflow volume is comparable in all models.

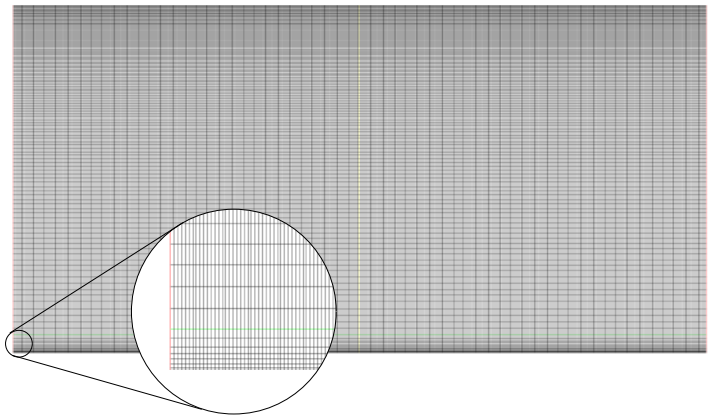

a)

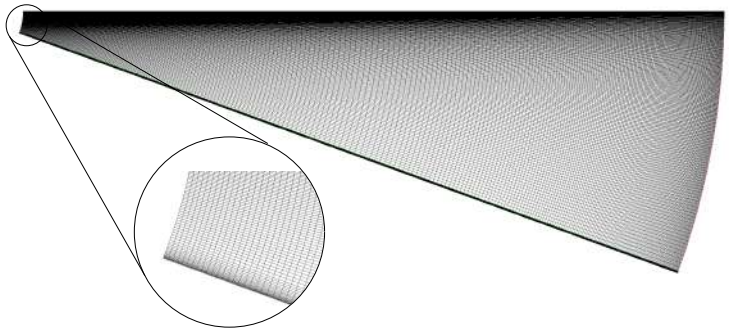

b)

Figure 4-5: Detail on meshes for simpler models. a) Mesh for model 1 has quadrilateral elements, a static zone over the tongue, and a smooth transition inflation with a grow rate of 1.2 over the tongue-boundary and the palate. b) Mesh for model 2 with quadrilateral elements

a)

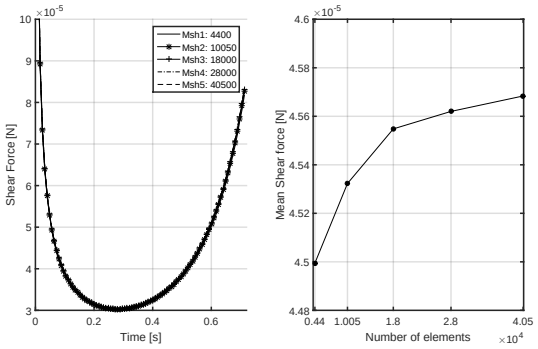

b)

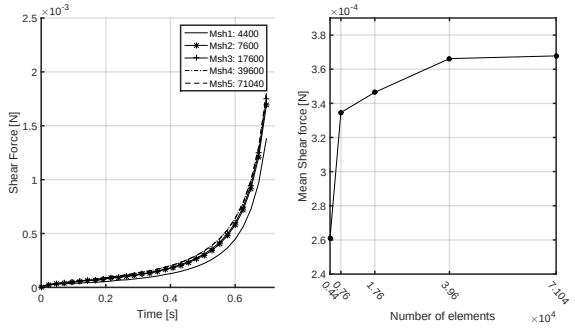

Figure 4-6: Convergence test for different meshes for each model: a) Model 1, b) Model 2

$$\begin{aligned} \bar{F} &= \int_0^{t_e} \int_{A_{tongue}} P \, dA dt / t_e \\ \bar{S_f} &= \int_0^{t_e} S_f \, dt / t_e \\ \bar{V} &= \int_0^{t_e} Q \, dt \end{aligned} \tag{4-1}$$

Where $t_e = 0.72[s]$, corresponds to the duration of the event under consideration.

	$\bar{F}$ [N]	$\bar{S_f}$ [N]	V [mL]
Model 1	4.29×10^{-4}	3.26×10^{-5}	18.06
Model 2	11.32×10^{-3}	13.97×10^{-5}	18.06
Model 3	13.98×10^{-3}	18.00×10^{-5}	18.17

Table 4-1: Computed integrals of time for all models using water.

Finally, it is remarkable that model 2 produces very similar results when compared with the physiological accurate behavior of model 3, even though the former simplifies tongue's motion as a rigid moving boundary. However, flow rate clearly shows a more complex fluid dynamics, which is also shown in the force and shear force plots in Figure **4-7**.

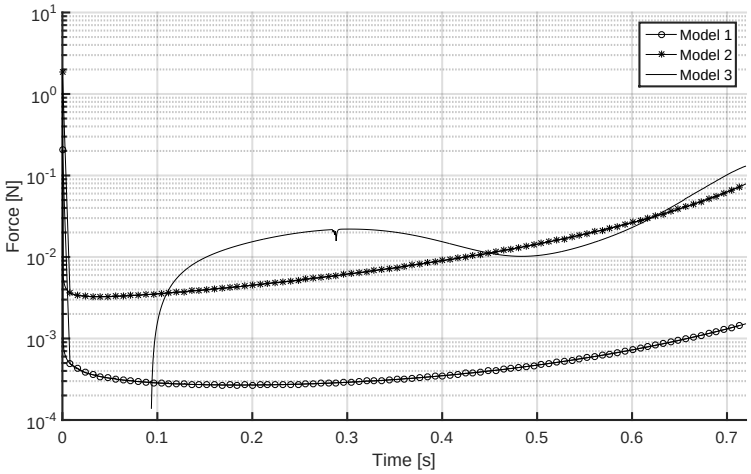

a)

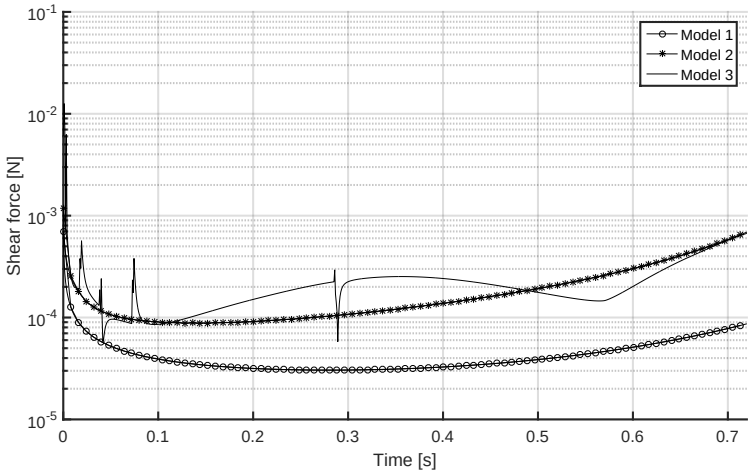

b)

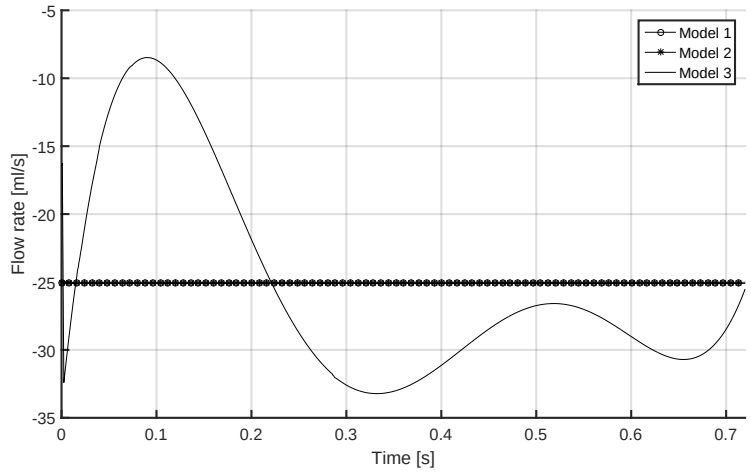

c)

Figure 4-7: Comparison of fluid variables for all models: a) force [N], b) shear force [N], c) flow rate [mL/s]

4.3 Experimental bench of oral swallowing

In order to further validate the simulations, an experimental bench that recreates the oral phase of swallowing was designed and constructed. The design of the device followed a top down design approach [33], starting off with the design requirements briefly described in the following section. The system was defined as a single phase continuum.

4.3.1 List of requirements for the experimental bench of oral swallowing

Seal-efficient, portability and cost were the main restrictions during the design, and additionally, it had to serve as validation to an *in-silico* model, or at the very least as an indirect validation, i.e. validate a numerical model that use the same procedure as the proposed in the previous chapter, but with different geometry and dimensions. Additionally, Particle Image Velocimetry (PIV) was selected as measurement technique, in order to obtain velocity fields and compare this property to ones obtained with numerical methods. The requirements of the experimental bench are listed below and are divided into functional and measurement requirements.

Functional requirements

- Recreate motion similar to the tongue's contour.
- Transport the fluid under consideration with the movement of the artificial tongue.
- Allow moving parts in a closed chamber without leaking.
- Provide seal at every time.
- Assured that the tank can be emptied completely.
- Allow complete disassemble.
- Prevent back-flow
- Maintain the assumption of single phase

Measurement requirements

- Provide a transparent visualization window to the moving tongue.
- Provide optical access to the fluid under consideration.
- Allow fluid flow with tracking particles.

4.3.2 Conceptual design of the experimental bench

From the requirements a conceptual experimental bench was sketched. The experimental bench was called "Artificial Tongue for Oral Swallowing (ATOS)".

ATOS V1 consists of three main components: artificial oral cavity, artificial tongue and sealing mechanism. The main components are composed on subcomponents as shown in Figure **4-8**. Detailed blue prints can be found in Appendix F.

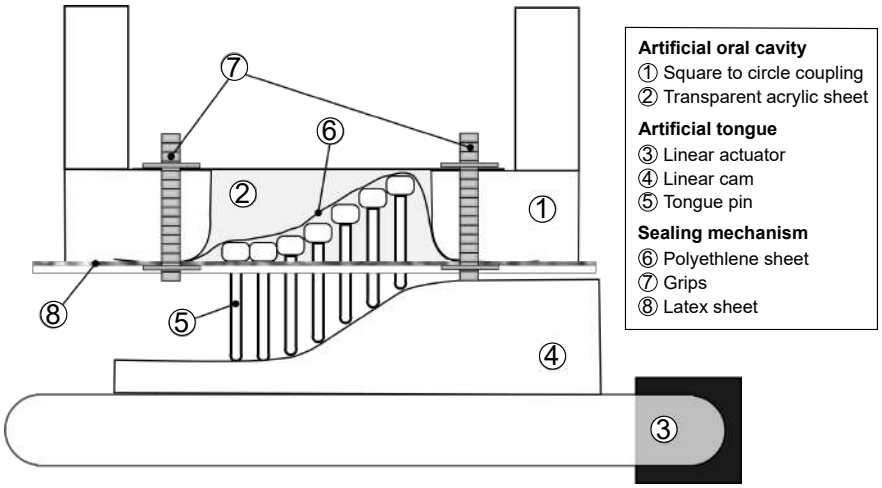

Figure 4-8: Conceptual representation of ATOS.

Artificial oral cavity

The oral cavity is a transparent acrylic box with 5 [mm] thickness composed of an upper and lower part, with a volume (Depth x Height x Width) of $60x45x146mm^3$. It also has two couplings to match the circular tubing to the square artificial oral cavity, which were made using additive manufacturing and were designed to reduce the pressure lost when changing the geometry. Silicone was used to complement the sealing between the acrylic box and the coupling.

Artificial tongue

The artificial tongue was composed of seven rod-followers that moved in a coordinate manner to imitate the motion of the tongue. The coordination is governed by a linear cam made of Ultra High Molecular Weight (UHMW) Polyethylene, which moves in the sagittal plane and was designed based on a cycloidal motion curve that vertically displaced the rods a distance of 32 mm in 0.66 s at a linear speed of 106 mm/s.

The rod-followers had a 'T' form with a rectangular block of Silicone Rubber ($60x8x10mm^3$) on top of their heads, see Figure **4-9**. They slid inside a rod block as their bottom tips followed the cam profile. However, additional latex sheets were implemented to restrict the rotation of the rods inside the rod block and to oblige the rods to return to the initial position and maintain the contact with the cam profile, see Figure **4-9.a.**. The latex restrains for the followers required grooves to reduce its stiffness since the linear actuator required more power to elevate the followers. The artificial tongue's contour was smoothed while preserving seal using a relaxed high density polyethylene sheet on top of the rubber heads, as seen in Figure **4-10**.

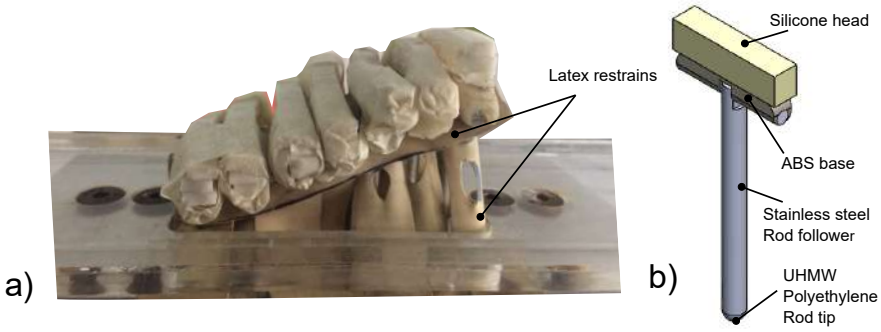

Figure 4-9: Detail on the head and assembly of the rod-followers. a) Lateral view of the rods. b) Isometric view of the rod assembly.

Sealing mechanism

A sheet of latex (thickness=0.36 mm) in between the upper and lower oral cavity was used as lateral, anterior and posterior sealing. Additionally, two grips were securely placed at both ends of the oral cavity to press the seal. It was found that the latex deteriorates when in contact with water for elongated time, and in turn would devilate the sealing mechanism. Therefore, it had to be inspected and dried after some experimental runs.

In the middle section, where the tongue resides, the latex sheet would have exerted a resistance to the vertical movement of the tongue. Therefore, we used instead the thin sheet of high density polyethylene as explained previously.

How it works

First, the fluid container fills the artificial oral cavity with the sealing mechanism, where the artificial tongue resides. The pouring of the liquid has to be made slowly and with an

Figure 4-10: Detail on HDPE sheet and the latex sheet on top of the rods. When the oral cavity is filled with the fluid, the sheet is compressed against the rod's head.

inclination, so that the free surface is at least at 50^o with respect to the inlet tube. Such procedure minimize the inlet of air into the system, but bubbles persisted to appear and purging methods must be implemented in future designs.

The artificial tongue is attached to seven evenly spaced rods with round tips that slides over a linear cam. As the linear actuator moves the cam forward and backward, the rods are moved vertically. Gravity is not enough to push them back down again, therefore, latex strips are attached to the rods heads and are held in place by the sealing grips.

Finally, the entrance is closed and the linear actuator in initialized. This moves the rods and in turn the tongue, displacing the fluid to the exit of the oral cavity. Once the stroke of the linear actuator is completed, the event is finished and the cam is pushed back. No measurement of the fluid dynamics when the cam returns is recorded nor measured.

4.3.3 Repeatability results for the experimental bench

A repeatability test was performed using water as testing fluid. The displaced volume in every stroke was collected and measured 40 times with a precision scale (HKD-6000B $d = 0.1g$). The results are shown in Figure **4-11**. During the test, the oral cavity was filled completely, the inlet was closed and the cam moved half a stroke at a speed of 106 mm/s.

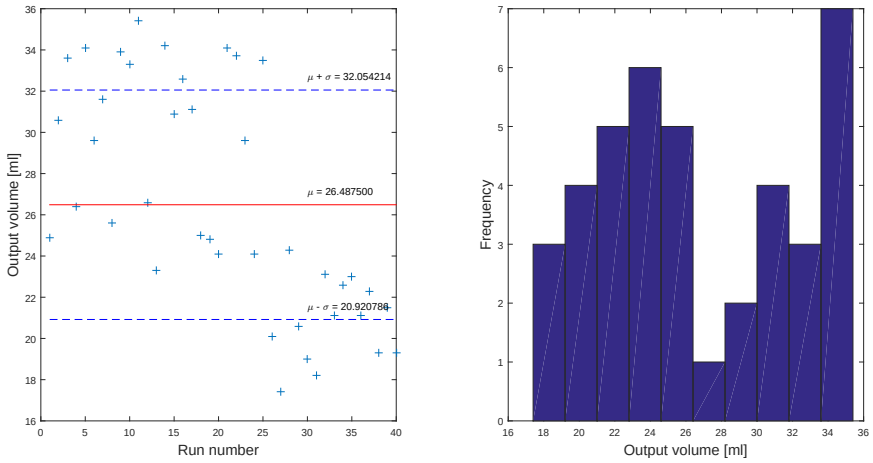

Figure 4-11: Distribution of the output volume measured in 40 complete runs.

The average output volume was 26.5 (5.6) [ml]. Such a result must be improved and the design of the experimental bench should be revised. During the test, as time advanced, the lateral seal weakened and the leaks began to alter the volume inside the oral cavity and this might have influenced the results. On the other hand, backward flow occurred in several runs and was especially sensible to the seal at the inlet tube and the level of water at the inlet. When a gap of air was left at the inlet, the backward flow was more evident.

4.4 Measurement with PIV

4.4.1 Experimental set up

The Figure **4-12** shows the experimental set-up for measuring velocity fields using PIV. It consists of a camera (CASIO ®EX-FH20, 30 frames per second [FPM], $f = 0.012[m]$, $f_{\#} = 2.8$, $ISO = 800$, shutter speed = 1/250, B/W), a laser ($continuous wave, \approx 1[W]$, $532 \pm 10[nm]$) and a cylindrical lens ($\varnothing = 6.02[mm]$).

The procedure was as follows: First the camera filmed perpendicular to the window of interest in the oral cavity. At the same time, the laser beam impacted the cylindrical lens and the latter transformed the beam into a laser sheet. The sheet of laser illuminated the sagittal plane of the oral cavity from above and the camera stored the reflection of the tracking particles that are immersed in the fluid. The images were later processed using PIVlab [54], where pre-processing filtering and cross-correlation took place.

After trial and error of probing several testing particles, graphite powder was chosen with a particle size of approximately $\varnothing = 45[\mu m]$, specific gravity $SG = 1.9$ and at a concentration

of $6E-6[kg/m^3]$. The size and concentration were found after trial and error, inspecting the results of the image processing technique.

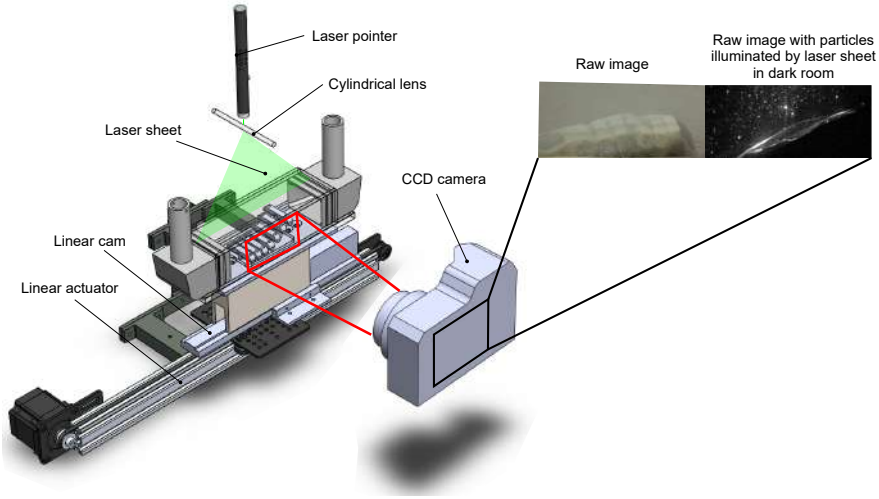

Figure 4-12: Experimental setup to measure using PIV technique with ATOS.

4.4.2 PIVlab workflow

PIVlab[54] was selected as analysis software, and as any other PIV processing software, its goal is to cross-correlate interrogation areas in the subsequent time frame, to estimate the direction and magnitude in which the particles moved from the previous time step. In this sense, they differ from Particle tracking velocimetry (PTV), in which individual particles are tracked frame to frame. The specific work flow in PIVlab used in this work is shown in Figure **4-13**, where there were five main phases: lecture of images, pre-processing and calibration of physical quantities in pixels, image cross-correlation, post-processing which involve manual cleaning of anomalies and interpolation, and finally, exporting the results.

On the other hand, the cross correlation must exclude the tongue's moving boundary region from the cross correlation analysis. Therefore, a mask over each tongue's contour for each frame had to be drawn manually. The latter was done instead of an automatic detection algorithm since the tongue's contour was difficult to identify due to the lack of contrast between the artificial tongue and the fluid, and also due to illumination variations between frames.

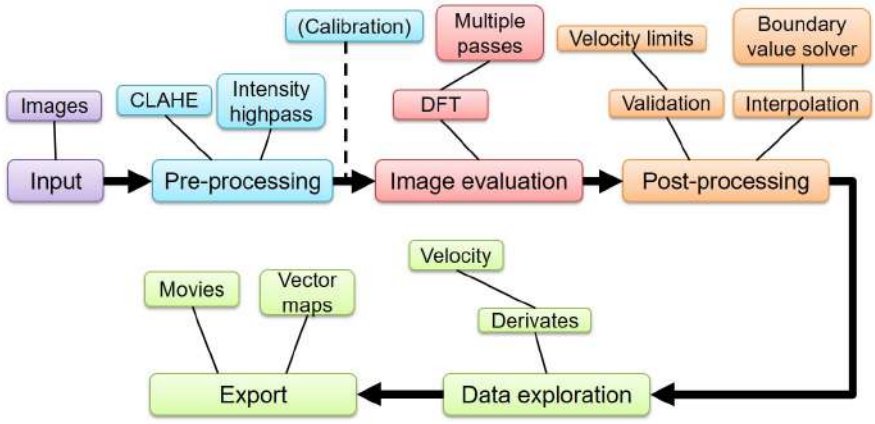

Figure 4-13: Summary of the steps taken within PIVlab to analyse the data from the images of the experimental bench. Modified from [54]

4.4.3 Image pre-processing parameters

First, the images had to be prepared using two filters, high-pass and wiener2 denoise filter, to compensate for illumination unevenness, over-illuminated particles and background noise. The Figure **4-14** shows the original image and the image with the filters applied. Notice how the contrast is incremented and the particles are more clearly defined. Additionally, the zoomed window shows that in general, the particles are constructed by 4 px each.

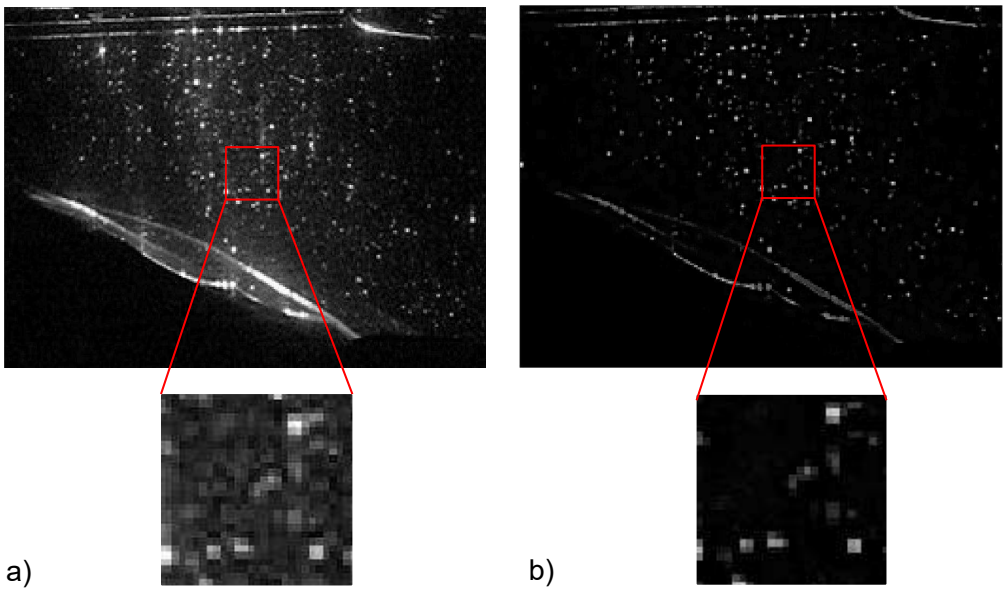

Figure 4-14: Frame 1 a) before and b) after Highpass Filter with 5 px and Wiener2 denoise filter with a window size of 5.

4.4.4 PIV settings

The video was separated in frames using MATLAB ®and 140 of them were selected, since they contained the movement of the artificial tongue. The settings used as image preprocessing inside PIVlab are summarized in Table **4-2**.

Table 4-2: PIVlab settings.

Setting	**Parameter**
ROI [px]	301x175
PIV algorithm	FFT window deformation
Int. area Pass 1 [px]	64x32
Int. area Pass 2 [px]	32x16
Win. Def. interpolator	linear
Sub-pixel estimator	2D Gauss

From the image acquired by the camera, a region of interest (ROI) was selected. Then, the cross correlation algorithm used was Fourier Fast Transformation, see [54], with two interrogation areas of decreasing size. The last two parameters in Table **4-2** were used for the interpolation of the velocity vectors.

It is worth noticing that before calculating the cross-correlation matrix, the program allowed to validate the magnitude of the velocity vectors to be calculated. That is, giving the ratio of pixels per millimeter and the time between frames. For our case, the ratio of pixels per millimeter was $px_{scale} = 0.0411mm/px$ and a time of $4.76ms$ between frames.

4.4.5 PIV results

The Figure **4-15** shows the velocity vectors for 6 discrete times from the 140 time frames, where the artificial tongue (masked region in red) displaced the fluid outward. As expected, the flow began with erratic displacements of particles, but as the flow developed, the direction of the velocity vectors were more uniform.

Using the PIV technique, under the conditions presented in the previous section, the mean value of velocity in all the domain for all time steps was 48.1(14.9) mm/s, which is in the same order of magnitude with the previous simulations. However, a more direct comparison with the experimental bench was done extracting the contour of the artificial tongue and simulating it in ANSYS FLUENT, with the same procedure as in section 3.1.4.

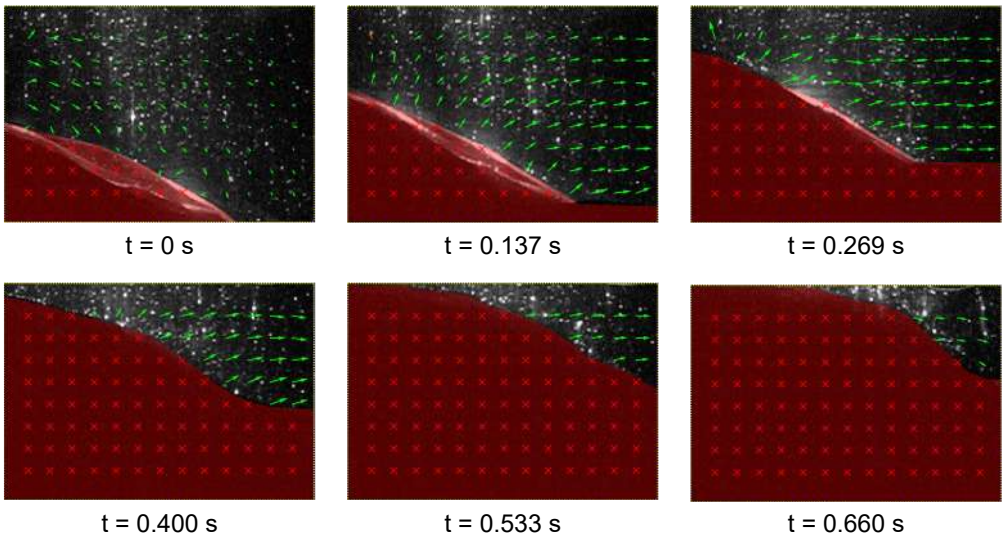

Figure 4-15: Calculated velocity field calculated and the evolution of the masked region.

As previously mentioned, the extraction of the masked region was done manually. Due to the same restrictions, the extraction of the tongue's contour for the simulation was done extracting the manually defined masked region, rather than using the raw images. The Figure **4-16** shows the implemented MATLAB ®algorithm to obtain the contour of the masked region. First, the red-masked zone, as shown in Figure **4-15**, was identified and isolated using YCbCr color filters; then, the contour was identified using the algorithm "bwboundaries", based on the Moore-Neighbor tracing algorithm modified by Jacob's stopping criteria [16]. Once the raw contour was identified, it had to be smoothed and then interpolated, see Appendix E for the complete code.

The domain for the simulation used the same boundary conditions as the ones used in model 3 in the previous chapter. Moreover, it also required dynamic mesh algorithms, specifically Remeshing and Smoothing, and had the same duration as the time used for PIV calculation, 0.66 s. However, the simulation used a temporal discretization of 1000 time steps, in contrast to the 140 frames from the PIV images.

From the simulation, a vector plot of the velocity field, see Figure **4-18**, showed a similar behavior as the one obtained from the PIV, however, from the time 0.528s onward, the fluid had a reverse flow, which was evident when inspecting the vector field, see Figure **4-17**. The origin of this reverse flow may be attributed to an expansion of the domain, obtained from the approximation of the tongue's boundary from the experimental bench.

In order to compare quantitatively these results, the velocities magnitudes at the outlet for PIV and the simulation are extracted and depicted in Figure **4-19**. Both functions showed a quadratic behavior with its peak at half the stroke, but the simulation had a change in the

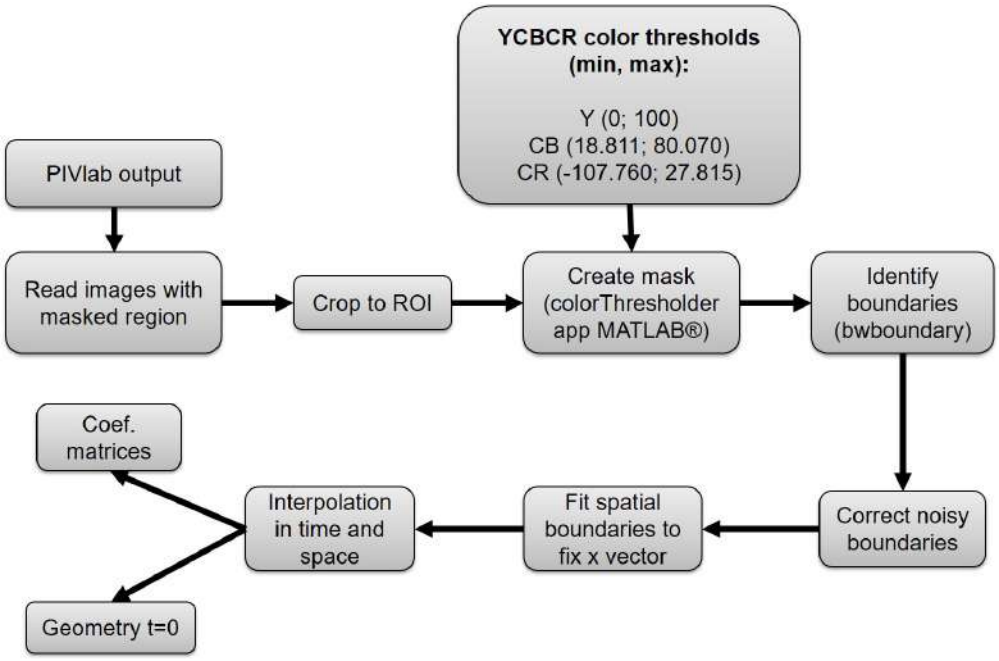

Figure 4-16: Algorithm implemented in MATLAB ®to extract the boundaries of the artificial tongue from ATOS.

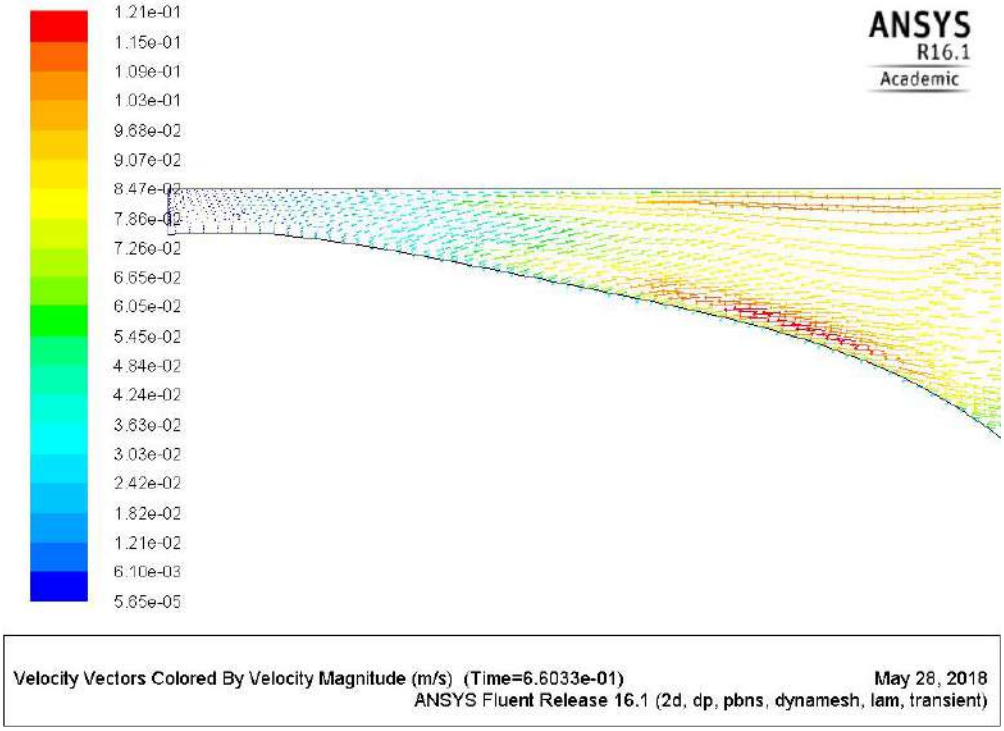

Figure 4-17: Vector field shows the backward flow experienced at the end of the simulation due to tongue's *dorsum* expansion.

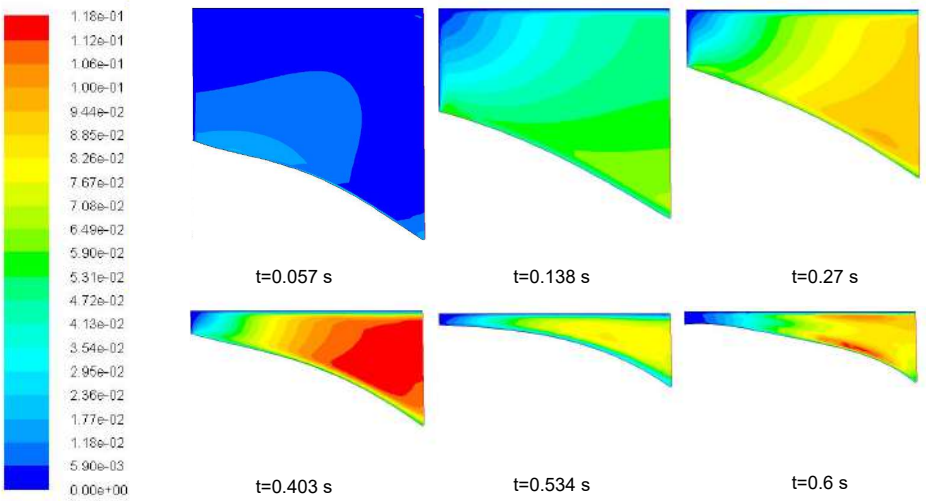

Figure 4-18: Calculated velocity field from simulations of the domain in ANSYS FLUENT.

slop at $0.6s$, which obeyed to the reverse flow.

The mean magnitudes of outlet velocity for both approaches were 48.1 mm/s and 65.4 mm/s, for the PIV and simulation approaches, respectively. The difference may attributed to experimental bench's and/or to limitation in the simulated model. On one side, there was deficiencies in the lateral seal, which did not work properly during the experiments and air bubbles entered the cavity. This must undoubtedly affected the internal pressure and in general the flow properties. Additionally, the simulated model considered only a fraction of the domain, and boundary errors may have influenced the results.

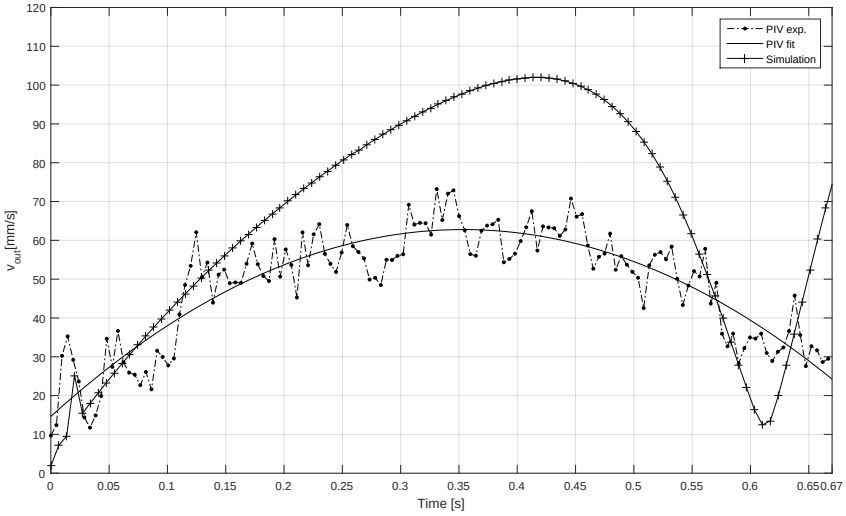

Figure 4-19: Average change in time of the outlet velocity calculated by the PIV technique in the ATOS experimental bench.

Conclusions and future works

5.1 Conclusions

Swallowing is a topic of interest for the research community since its malfunction affects heavily the life quality of people and it is originated as collateral damage from several diseases. *In-silico* models are attractive since they allow the design of experiments with a wide range of test parameters without affecting an actual patient. However, the models presented in the state of the art were difficult to compare to one another and lack validation approaches.

This work intented to close the breach between simplified models, such as the ones from [42] and [10], with more complex, three dimensional and more physiological accurate models such as [21]. To this end, this work developed and numerically implemented a procedure to transfer the tongue's contour dynamics from RT-MRI into a CFD commercial software, and with this, implement a physiological precise numerical model.

This model, in its dimensional and non-dimensional form, offer detailed information on the food bolus' dynamics during the oral phase of swallowing. However, large deformations on the fluid domain were originated by the tongue's contour, and as far as the author could verify, no previous work had ventured to use a moving boundary to this extended, using polynomial fittings to control the boundary. Therefore, the results should be revised with care since numerical artifices were found in some iterations and may be attributed to the use of the user defined function and/or dynamic mesh algorithms.

The procedure to establish the correct parameters for dynamic mesh algorithms was trial and error, and its implementation demand fine temporal discretization. Otherwise, negative volume error occurred frequently. These parameters are mesh dependent, therefore, the convergence analysis was inconvenient and took special care to detail.

The negative results of force as a function of time for model 3 in the first 100 time steps (1/9 th of the total simulation time) for fluids with low viscosity were attributed to local reverse flow near the tongue boundary as a result of poor layer height in the vicinity. We

hypothesized that rapid expansion-compression in the moving domain were responsible for this reverse flow. Although, this expansion was the natural movement from the patient's RT-MRI, the extrapolation to swallowing physiology should be revised with caution due to model's numerical limitations.

From the design of experiments for model 3, it can be concluded that density showed no relevance in the output flow rate, output velocity, nor the shear force over the tongue; on the other hand, the time of event and the viscosity showed a marked influence in all the evaluated output variables. In regard to the interactions between factors, it was found that event time and viscosity do not sum their effects.

Even though, these results could predict orders of magnitudes for forces and flow rate during oral swallowing, they were still depended on the geometry of one patient, therefore, a dimensionless model was formulated. Such model evaluated force coefficient and friction coefficient as a function of Reynolds number. When these functions were plotted, the simulations were sorted according to the event time, and each individual group followed an exponential decay function. Lower Reynolds numbers and faster swallowing implied larger force and friction coefficients. We expect that this model could serve as a predictive model to estimate force and friction parameters of swallowing from rheological parameters and swallowing habits, but still requires validation with additional RT-MRI that can be processed with the same procedure.

To this point, model 3 was promising, but presented two challenges: There was no certainty whether moving boundary in classic CFD was a suitable and reliable method to displace a fluid and whether the magnitudes of the numerical model resemble the ones encounter in *in-vivo* swallowing. Therefore, different validation approaches were tackled.

To test the moving boundary, two additional models, with geometries taken from literature, were modeled using CFD as well. The approach was the same as with model 3, where the fluid flow is driven by the tongue's movement and not by a force exerted by the tongue's boundary, as was the case in [42]. With our approach, the models were comparable with each other, as long as the magnitude of change in volume and duration of the event held the same.

Moreover, model 2 presented close results to the results of force and shear force of model 3, even though the tongue's dynamics was simplified. On the other hand, model 1 presented one and two order of magnitude of difference in force and shear force over the tongue, with respect to the other two models. Therefore, model 1 relevance as swallowing model should be revised, since its geometry might be over-simplified. However, the inclusion of partial slip [44] should be considered in more complex models.

In order to evaluate the order of magnitude with respect to an *in-vivo* test, the centroid of the food bolus in the *in-vivo* data from the RT-MRI was tracked using image processing techniques, showing promising results with similar orders of magnitude as the simulation. However, the images' quality affected the precision of image processing techniques and the centroid presented atypical movement that can be attributed to noise in the images. Therefore,increased image resolution and shutter speed in RT-MRI might improve the overall result. This approach is an automation of a manual protocol used by phonologist, in which they manually "track" the head/tail of the food bolus to determine its velocity, and this tracking algorithm should be considered for implementation, once the acquisition of images is refined. The main drawback of such procedure is that it can only show the velocity of the food bolus as a rigid body (particle tracking), but the RT-MRI technique should also consider the use of particles within the contrast fluid of the procedure, that might allow the implementation of Particle Tracking Velocimetry (PTV) or even Particle Image Velocimetry (PIV) techniques.

Finally, a novel experimental bench of oral swallowing was designed and constructed, since no moving boundary experimental bench was found in literature. Additionally, in order to measure the fluid's dynamics, a homemade PIV set up was implemented. There were many limitations, from the bench and from the homemade PIV setup, alike. On one side, the sealing mechanism must be improved, since it might have affected pressure inside the oral cavity, and the resolution of the images and camera's lens sensibility to light must be improved in future setups. The graphite particles behaved surprisingly well for low velocity flows and benchmark experiments should test the extend to which this material can be used as contrast particle. Additionally, commercial cylindrical lenses might allow a more efficient transition from the laser to the laser sheet, but the one used in this setup was sufficient.

Even though, low accuracy was anticipated with a repeatability test, both qualitative and quantitative results were achieved, with modest similarities between the PIV results and the simulations. The order of magnitude and function behavior was held, but the simulation results doubled the ones obtained from the PIV.

5.2 Future works

The physiological accurate model presented in this work is the first step towards a more complex model, but has several limitations. The most fundamental of all is the assumption of domain's sagittal geometry generality since the model was based on only one patient. Therefore, a future work should apply the same procedure to other patients' RT-MRI and compare the difference in the sagittal tongue's contour dynamics and the subsequent food bolus' dynamics.

Additionally, future works could explore the use of partial slip boundary condition and non Newtonian fluids in depth, which resemble more complex rheological properties of food bolus. Additionally, future works should consider suspended particles in food bolus and no continuous fluids. The latter however would require alternative methods of numerical fluid flow analysis such as meshless methods.

This work considered the behavior of the food bolus as it is propelled by the movement of the tongue. However, it did not consider how the food bolus affected the tongue, i.e. the fluid structure interaction between them, which can be one way or two way.

Finally, a three dimensional model could be devised, under the same premise of physiological accurate movement, using three dimensional dynamic resonance imaging, or similar techniques. Such a model could be directly compare with full three dimensional models already in literature, see Section 2.2.4, that used different solver approaches, other than computer fluid dynamics.

In regard to the experimental bench, ATOS can be improved in several ways. On one side, thinner and numerous pins would allow a finer discretisation of tongue's dynamics, using the same actuation mechanism. Furthermore, the use of pneumatic actuators or individual cams for each pin can recreate more complex and accurate tongue's contour, and were not used in this work due to budget limitations. The proposed sealing mechanism was proved to be ineffective and additional experimental bench should consider that as a top priority requirement.

Future experimental bench should also consider specially designed check valves, that allow the free transit of contrast particles, and a mechanism to retrieve them downstream. Furthermore, in order to improve the stability of the system, alternative mechanism to connect the oral cavity with the linear actuator should be devised, since the current mechanism allow clearance and vibrations that are reflected on the flow's dynamics.

On the other side, future works should test the extend to which the homemade PIV can be used to determine flow's dynamics. In order to test low velocity flows, the use of continuous-wave laser was sufficient but more accurate results can be achieve synchronizing the shutter from the camera with a pulsed laser.

Bibliography

[1] Neil Bhattacharyya. The prevalence of dysphagia among adults in the united states. *Otolaryngology-Head and Neck Surgery*, 151(5):765–769, 2014. PMID: 25193514.

[2] M W Chang, B Rosendall, and B A Finlayson. Mathematical modeling of normal pharyngeal bolus transport: a preliminary study. *Journal of rehabilitation research and development*, 35(3):327–34, Jul 1998.

[3] Julie Cichero, Timothy Nicholson, and Pamela Dodrill. Liquid barium is not representative of infant formula: characterisation of rheological and material properties. *Dysphagia*, 26(3):264–71, Sep 2011.

[4] Ian J Cook, Wylie J Dodds, Roberto O Dantas, Mark K Kern, Benson T Massey, Reza Shaker, and Walter J Hogan. Timing of videofluoroscopic, manometric events, and bolus transit during the oral and pharyngeal phases of swallowing. *Dysphagia*, 4(1):8–15, 1989.

[5] Clement De Loubens, Albert Magnin, Marion Doyennette, Ioan Trelea, and Isabelle Souchon. A biomechanical model of swallowing for understanding the influence of saliva and food bolus viscosity on flavour release. *Journal of theoretical biology*, 280:180–8, 07 2011.

[6] Clément de Loubens, Albert Magnin, Eric Verin, Marion Doyennette, Ioan Cristian Tréléa, and Isabelle Souchon. A lubrication analysis of pharyngeal peristalsis: application to flavour release. *Journal of theoretical biology*, 267(3):300–11, Dec 2010.

[7] Gabriel J. DeSalvo and John A. Swanson. *Ansys Fluent 12.0 User manual*. Ansys, Inc., Dassault Systemes, 1 edition.

[8] Michael S Engelman. FIDAP (a fluid dynamics analysis program). *Advances in Engineering Software (1978)*, 4(4):163–166, oct 1982.

[9] Jan Engmann, Colin Servais, and Adam Burbidge. Squeeze flow theory and applications to rheometry: A review. *Journal of Non-newtonian Fluid Mechanics*, 132:1–27, 12 2005.

[10] Carol Fairfield. Mathematical modelling of the normal swallow. Report on a problem studied at the UK Mathematics-in-Medicine Study Group Strathclyde 2010.

[11] Moshiur Rahman Farazi, Bonnie Martin-Harris, Negar M Harandi, Sidney Fels, and Rafeef Abugharbieh. A 3d dynamic biomechanical swallowing model for training and diagnosis of dysphagia. In *Biomedical Imaging (ISBI), 2015 IEEE 12th International Symposium on*, pages 1385–1388. IEEE, 2015.

[12] Gad Friedman. Esophagus function. url = http://tenderness.co/esophagus-function/, Dec 2017.

[13] Satoru Fujita, Jianwu Dang, Noriko Suzuki, and Kiyoshi Honda. A computational tongue model and its clinical application. *Oral Science International*, 4(2):97 – 109, 2007.

[14] Yuan-Cheng Fung. Biomechanics: Mechanical properties of living tissues. In *Biomechanical models for soft tissue simulation*, chapter 9, pages 392–426. Springer New York, 1993.

[15] Jean-Michel Gerard, Jacques Ohayon, Vincent Luboz, Pascal Perrier, and Yohan Payan. Indentation for estimating the human tongue soft tissues constitutive law: Application to a 3d biomechanical model. *Springer-Verlag*, 1:77–83, 2004.

[16] Rafael C Gonzalez, Richard E Woods, and Steven L Eddins. *Digital image processing using MATLAB*, volume 2. Gatesmark Publishing Knoxville, 2009.

[17] Robert M. Haralick and Linda G. Shapiro. *Computer and Robot Vision*. Addison-Wesley Longman Publishing Co., Inc., Boston, MA, USA, 1st edition, 1992.

[18] P. Hayoun, J. Engmann, S. Mowlavi, B. Le Reverend, A. Burbidge, and M. Ramaioli. A model experiment to understand the oral phase of swallowing of newtonian liquids. *Journal of biomechanics*, 48:3922–3928, 2015.

[19] The American Heritage. The american heritage science dictionary, Dec 2017.

[20] Charles Hirsch. *Numerical Computation of Internal and External Flows, Volume 2: Computational Methods for Inviscid and Viscous Flows*. Wiley, 1990.

[21] Andrew Kenneth Ho, Ling Tsou, Sheldon Green, and Sidney Fels. A 3d swallowing simulation using smoothed particle hydrodynamics. *Computer Methods in Biomechanics and Biomedical Engineering: Imaging & Visualization*, 2(4):237–244, 2014.

[22] K Hori, H Hayashi, S Yokoyama, T Ono, S Ishihara, J Magara, H Taniguchi, T Funami, Y Maeda, and M Inoue. Comparison of mechanical analyses and tongue pressure analyses during squeezing and swallowing of gels. *Food hydrocolloids*, 44:145–155, 2015.

[23] P J Kahrilas, S Lin, J Chen, and J A Logemann. Oropharyngeal accommodation to swallow volume. *Gastroenterology*, 111(2):297–306, Aug 1996.

[24] Hak N. Kim, Jan S. Lewin, Jodi K. Knott, Katherine A. Hutcheson, and Alexander Dekovich. Novel therapeutic approach to relieve pharyngoesophageal spasm after total laryngectomy. *Gastrointestinal Endoscopy*, 76(1):193–196, jul 2012.

[25] Scott A. King and Richard E. Parent. *A Parametric Tongue Model for Animated Speech*, chapter 1, pages 3–13. Springer Vienna, Vienna, 2000.

[26] W. Kou, B. E. Griffith, J. E. Pandolfino, P. J. Kahrilas, and N. A. Patankar. A musculo-mechanical model of esophageal transport based on an immersed boundary-finite element approach. In *APS Meeting Abstracts*, November 2015.

[27] Wenjun Kou, Amneet Pal Singh Bhalla, Boyce E. Griffith, John E. Pandolfino, Peter J. Kahrilas, and Neelesh A. Patankar. A fully resolved active musculo-mechanical model for esophageal transport. *Journal of Computational Physics*, 298:446–465, oct 2015.

[28] Martin Kroger, Editors@Appliedrheology.Org, and Editor Applied Rheology. "a day in the life of the fluid bolus": An introduction to fluid mechanics of the oropharyngeal phase of swallowing with particular focus on dysphagia. *Applied Rheology; ETH Zurich*, pages 1–10, 2016.

[29] Mathieu Labrunie, Pierre Badin, Dirk Voit, Arun A Joseph, Jens Frahm, Laurent Lamalle, Coriandre Vilain, and Louis-Jean BoÃ≪. Automatic segmentation of speech articulators from real-time midsagittal MRI based on supervised learning. *Speech Communication*, 99:27–46, may 2018.

[30] Jeri A. Logemann. Evaluation and treatment of swallowing disorders. *NSSLHA Journal*, 1:38–53, 1984.

[31] Negar M. Harandi. 3d segmentation of the tongue in mri: a minimally interactive model-based approach. *Computer Methods in Biomechanics and Biomedical Engineering: Imaging and Visualization*, 02 2014.

[32] M. R. Mackley, C. Tock, R. Anthony, S. A. Butler, G. Chapman, and D. C. Vadillo. The rheology and processing behavior of starch and gum-based dysphagia thickeners. *Journal of Rheology*, 57(6):1533–1553, nov 2013.

[33] M. Mantyla. A modeling system for top-down design of assembled products. *IBM Journal of Research and Development*, 34(5):636–659, Sept 1990.

[34] Bonnie Martin-Harris and Bronwyn Jones. The videofluorographic swallowing study. *Physical Medicine and Rehabilitation Clinics of North America*, 19(4):769–785, nov 2008.

[35] Koichiro Matsuo and Jeffrey B. Palmer. Coordination of mastication, swallowing and breathing. *Japanese Dental Science Review*, 45:31–40, 2009.

[36] Mary L. McHugh. The chi-square test of independence. *Biochemia Medica*, pages 143–149, 2013.

[37] Y. Meng, M.A. Rao, and A.K. Datta. Computer simulation of the pharyngeal bolus transport of newtonian and non-newtonian fluids. *Food and Bioproducts Procedings*, 83:297–305, 2005.

[38] J.C. Misra and S.K. Pandey. A mathematical model for oesophageal swallowing of a food-bolus. *Mathematical and computer modelling*, 33:997–1009, 2001.

[39] H. Mizunuma, M. Sonomura, K. Shimokasa, H. Ogoshi, S. Nakamura, and N. Tayama. Numerical modeling and simulation on the swallowing of jelly. *Journal of Textures Studies*, 40:406–426, 2009.

[40] S Mossaz, P Jay, and Magnin A. Rhéologie et étalement du bol alimentaire dans la cavité buccale. *Rhéologie and thermodynamique*, 1:79 – 82, 2008.

[41] Nestle. Swallowing difficulty is a common health issue and much can be done to manage symptoms and improve wellbeing. Accessed: 2018-13-01.

[42] M A Nicosia and J A Robbins. The fluid mechanics of bolus ejection from the oral cavity. *Journal of biomechanics*, 34(12):1537–44, Dec 2001.

[43] Mark A Nicosia. A planar finite element model of bolus containment in the oral cavity. *Computers in biology and medicine*, 37(10):1472–1478, 2007.

[44] Mark A. Nicosia. Theoretical estimation of shear rate during the oral phase of swallowing: effect of partial slip. *Journal of Textures Studies*, 44:132–139, 2012.

[45] Mark A Nicosia and James G Brasseur. A mathematical model for estimating muscle tension in vivo during esophageal bolus transport. *Journal of theoretical biology*, 219(2):235–55, Nov 2002.

[46] Kaori Nishikubo, Kazuyo Mise, Misato Ameya, Kahori Hirose, Taisuke Kbayashi, and Masamitsu Hyodo. Quantitative evaluation of age-related alteration of swallowing function: Videofluoroscopic and manometric studies. *Auris Nasus Larynx*, 42:134–38, 2015.

[47] Barbara R. Pauloski. Rehabilitation of dysphagia following head and neck cancer. *Physical Medicine and Rehabilitation Clinics of North America*, 19(4):889–928, nov 2008.

[48] Charles S Peskin. Numerical analysis of blood flow in the heart. *Journal of Computational Physics*, 25(3):220 – 252, 1977.

[49] Brigette M. Rosendall, Bruce A. Finlayson, and Michael W. Chang. A mathematical model for estimating muscle tension in vivo during esophageal bolus transport. *Tenth International conference on finite elements in fluids*, 10(2):118–123, Nov 1998.

[50] Y. Kuang S. Wienbaum, C.J. Lawrence. The inertial draining of a thin fluid layer between parellel plates with constant normal force. partq. analytic solutions; inviscid and small but finite reynolds-number limits. *Journal of Fluid Mechanics*, 156:463–477, 1985.

[51] Pierre Soille. *Morphological image analysis: principles and applications*. Springer-Verlag New York, Inc., 2003.

[52] Ian Stavness, John Lloyd, Yohan Payan, and Sidney Fels. Dynamic hard-soft tissue models for orofacial biomechanics. In *ACM SIGGRAPH Talks*, page 1, 2010.

[53] M E J Terpstra, A M Janssen, and E van der Linden. Exploring imperfect squeezing flow measurements in a teflon geometry for semisolid foods. *Journal of food science*, 72(9):E492–502, Nov 2007.

[54] William Thielicke and Eize J. Stamhuis. PIVlab – towards user-friendly, affordable and accurate digital particle image velocimetry in MATLAB. *Journal of Open Research Software*, 2, oct 2014.

[55] Dharmendra Tripathi. A mathematical model for the movement of food bolus of varying viscosities through the esophagus. *Acta Astronautica*, 69(7):429–439, Sept 2011.

[56] Lenie van den Engel-Hoek, Imelda J M de Groot, Eva Esser, Birthe Gorissen, Jan C M Hendriks, Bert J M de Swart, and Alexander C H Geurts. Biomechanical events of swallowing are determined more by bolus consistency than by age or gender. *Physiology & behavior*, 106(2):285–90, May 2012.

[57] H. Versteeg and W. Malalasekera. *An Introduction to Computational Fluid Dynamics: The Finite Volume Method (2nd Edition)*. Pearson, 2 edition, 2007.

[58] WHO. *International Classification of Diseases (ICD)*. Geneva, Switzerland: WHO, 10 edition, 2016.

[59] Azizollaah Zargaraan, Reza Rastmanesh, Ghasem Fadavi, Farid Zayeri, and Mohammad Amin Mohammadifar. Rheological aspects of dysphagia-oriented food products: A mini review. *Food Science and Human Wellness*, 2(3):173 – 178, 2013.

Appendix: Computer Fluid Dynamics

A.1 Computational fluid dynamics

There are several approaches to solve the equations described. However due its flexibility, affinity with the governing equations, conservative discretization and extended use in commercial computational fluid dynamics (CFD) programs[57], the Finite Volumes Method (FVM) was selected as solution strategy.

The first step of this method is the grid generation, where the fluid domain is divided into several smaller sub-domains Ω_j, called cells or finite volumes. A control volume is to be defined around each finite volume and the physical boundaries coincide with the boundaries of the cells.

Next, consider the conservative equation of a transport quantity ϕ in the general form Equation A-1. Notice that the governing equations, presented in the previous section, were derived from this equation, taking $\phi = 1$ and $\phi = \mathbf{u}$ for mass and momentum conservation equations, respectively.Additionally, a third conservation equation, corresponding to the energy conservation, appears for $\phi = E$.

$$\rho\frac{\partial\phi}{\partial t} + \nabla\cdot(\rho\phi\mathbf{u}) = -\nabla P + \nabla\cdot(\Gamma\nabla\phi) + S_\phi \tag{A-1}$$

Where Γ is a diffusion coefficient (e.g.viscosity). Now, these equations are integrated over each control volume and then the divergence theorem is applied to obtain Equation A-2 [57].

$$\rho\frac{\partial}{\partial t}\int_{CV}\phi dV + \int_A \mathbf{n}\cdot(\rho\phi\mathbf{u})dA = \int_A \mathbf{n}\cdot(\Gamma\nabla\phi)dA + \int_{CV} S_\phi dV \tag{A-2}$$

This equation can be mathematically manipulated and grouped in vectors to obtain the form in Equation A-3.

$$\frac{\partial}{\partial t}\int_{CV}\mathbf{W}dV + \oint[\mathbf{F}-\mathbf{G}]\cdot dA = \int_{CV}\mathbf{H}dV \tag{A-3}$$

Where the vectors $\mathbf{W}$, $\mathbf{F}$, $\mathbf{G}$ are,

$$\mathbf{W} = \begin{pmatrix} \rho \\ \rho u \\ \rho v \\ \rho E \end{pmatrix}, \mathbf{F} = \begin{pmatrix} \rho\mathbf{u} \\ \rho\mathbf{u}u + P\hat{\imath} \\ \rho\mathbf{u}v + P\hat{\jmath} \\ \rho\mathbf{u}E + P\mathbf{u} \end{pmatrix}, \mathbf{G} = \begin{pmatrix} 0 \\ \boldsymbol{\tau}_x \\ \boldsymbol{\tau}_y \\ [\boldsymbol{\tau}] \cdot \mathbf{u} \end{pmatrix}$$

and $\mathbf{H}$ contains S_ϕ. Here E is total energy per unit mass and $[\boldsymbol{\tau}]$ is the viscous stress tensor.

The discretization of such these equations depend on the problem at hand. For this case, it was considered a two dimensional unsteady convective-diffusive case.

A.1.1 Spatial and temporal discretization schemes

For the discretization of Equation A-3, a pseudo-time-derivative is introduced for the time-marching procedure [7]. Using backward difference in time, the implicit in time formulation in semi-discrete form with first-order accuracy is shown in Equation A-4,

$$\left[\frac{\Gamma}{\Delta\tau} + \frac{\epsilon_0}{\Delta t}\frac{\partial \mathbf{W}}{\partial \mathbf{Q}}\right]\Delta\mathbf{Q}^{k+1} + \frac{1}{V}\oint[\mathbf{F} - \mathbf{G}] \cdot d\mathbf{A} = \mathbf{H} - \frac{1}{\Delta t}\left(\epsilon_0\mathbf{W}^k - \epsilon_1\mathbf{W}^n + \epsilon_2\mathbf{W}^{n-1}\right) \quad \text{(A-4)}$$

where $\epsilon_0 = \epsilon_1 = 1/2, \epsilon_2 = 0$. Using the implicit time-marching algorithm, the pseudo-time-derivative is driven to zero at each physical time step by inner iterations [7].

On the other hand, the spatial discretization corresponds to the creation of the mesh for the fluid domain, in which each cell's face contains the gradient of several fluid flow variables. The communication between cells, i.e. how the gradient of a certain variable is transferred to the next cell, must fulfilled the constitutive equations of previous sections. The most used discretization and interpolation schemes are central differencing scheme for the diffusive term, and a first order upwind scheme for the convective term. For more information refer to [57].

A.2 Dynamic mesh

The problem at hand has the particularity that the fluid domain changes its volume as the time advances, since the tongue moves toward the palate and propels the food bolus in between, with this movement. The mesh is therefore considered a dynamic mesh.

There are several dynamic mesh algorithms, the most used in commercial software are: layering, smoothing and remeshing. In layering, the algorithm collapses or divide cells adjacent to a moving boundary when these achieving a certain trigger value, .e.g 40% of cell height.

This algorithm is limited to meshes with wedges or hexahedra (quadrilaterals in 2D) elements in the boundary adjacent to the movement. See Figure A.2**.a**.

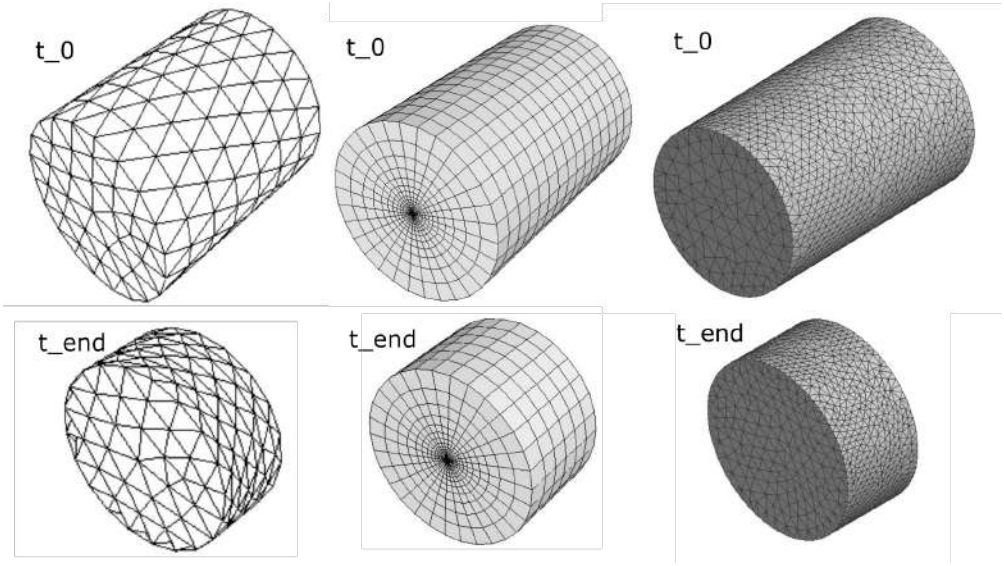

Figure A-1: Graphical representation of the dynamic mesh algorithms available in the commercial software Fluent ANSYS. a) Layering, b) Smoothing and c) remeshing. Source: Modified from [7].

The second method, smoothing, relaxes the meshes imposing relations to the edges between nodes. Such relations can follow Hooke's Law, therefore the edges are considered springs (Spring based Smoothing), or location adjustment of each mesh vertex to the geometric center of its neighboring vertices (Laplacian Smoothing). The latter does not guarantee the cell skewness in each new iterations, therefore is restricted when the skewness of the new element is not better or at least equal to the previous one. As seen in Figure A.2**.b**, the number of elements is conserved.

Finally, Figure A.2**.c.** shows the remeshing method which identifies the cells or faces that have been degenerated beyond minimum skewness or size criteria, and then locally re-meshes the cells or faces (generate new cells or faces), interpolating the previous nodes location. For more information please refer to [7].

Appendix: UDF used in ANSYS Fluent for physiological accurate movement

```
#include "udf.h"
#include "unsteady.h"
#include <stdio.h>
#include <stdlib.h>
#include <malloc.h>
#define rows 7
#define cols 7
#define nTime 1000
#define nSpatial 351

FILE *file1;
FILE *file2;
FILE *file3;
FILE *file4;
FILE *file5;
FILE *file6;

DEFINE_GRID_MOTION(tongueMov,domain,dt,time,dtime)
{
  //Fluent variables declaration
  Thread *tf = DT_THREAD(dt);
  face_t f;
  Node *v;
  real NV_VEC(A);
  int n;
  real NV_VEC(displ);

  //Algorithm variables declaration
  int i, j, k, x, tt, nk[nSpatial], count;
  double timeFix[nTime], spatialFix[nSpatial];
  double tempCoefy[cols], tempCoefx[cols], tempCoefTx[rows], tempCoefTy[rows];

////////////////////////////////////////////////////////////////////////////
```

```
    //Declare matrices
    double coefx[rows][cols];
    double coefy[rows][cols];
    double coefTx[cols][nSpatial];
    double coefTy[cols][nSpatial];
    double x_fit[nSpatial][nTime];
    double y_fit[nSpatial][nTime];

////////////////////////////////////////////////////////////////////////////////
    //Call and store coefy
    file1=fopen("coefy.txt", "r");
    for(i = 0; i < rows; i++)
    {
        for(j = 0; j < cols; j++)
        {
            if (!fscanf(file1, "%lf", &coefy[i][j]))
            {
               break;
            }
        }
    }
    fclose(file1);

    //Call and store coefx
    file2=fopen("coefx.txt", "r");
    for(i = 0; i < rows; i++)
    {
        for(j = 0; j < cols; j++)
        {
            if (!fscanf(file2, "%lf", &coefx[i][j]))
            {
              break;
            }
        }
    }
    fclose(file2);

    //Call and store parameters k
    file3=fopen("k.txt", "r");
    for(i = 0; i < nSpatial; i++)
    {
            if (!fscanf(file3, "%d", &nk[i]))
            {
              break;
            }
    }
    fclose(file3);

```

```
82 ////////////////////////////////////////////////////////////////////////////
83     //Define fix vectors linspaces
84     for(i=0;i<nTime;i++)
85     {
86         timeFix[i] = (double)(i) / ((double)(nTime)-1.0);
87     }
88     for(i=0;i<nSpatial;i++)
89     {
90         spatialFix[i] = (double)(i) / ((double)(nSpatial)-1.0);
91     }
92 
93 ////////////////////////////////////////////////////////////////////////////
94     // Eval polynom spatial
95     for (k = 0; k < nSpatial; k++)
96     {
97         for (i = 0; i < cols; i++)
98         {
99             for (j = 0; j < rows; j++)
100             {
101                 tempCoefx[j] = coefx[i][j];
102             }
103             coefTx[i][k] = tempCoefx[0];
104             for (count = 1; count <= cols-1; count++)
105             {
106                 coefTx[i][k] = coefTx[i][k]*spatialFix[k] + tempCoefx[count];
107             }
108         }
109     }
110     for (k = 0; k < nSpatial; k++)
111     {
112         for (i = 0; i < cols; i++)
113         {
114             for (j = 0; j < rows; j++)
115             {
116                 tempCoefy[j] = coefy[i][j];
117             }
118             coefTy[i][k] = tempCoefy[0];
119             for (count = 1; count <= cols-1; count++)
120             {
121                 coefTy[i][k] = coefTy[i][k]*spatialFix[k] + tempCoefy[count];
122             }
123         }
124     }
125 
126 ////////////////////////////////////////////////////////////////////////////
127     // Eval polynom temporal
128     for (k = 0; k < nTime; k++)//nTime
129     {
```

```
130         for (j = 0; j < nSpatial; j++)//nSpatial
131         {
132             for (i = 0; i < rows; i++)
133             {
134                 tempCoefTx[i] = coefTx[i][j];
135             }
136             x_fit[j][k] = tempCoefTx[0];
137             for (count = 1; count <= rows-1; count++)
138             {
139                 x_fit[j][k] = x_fit[j][k]*timeFix[k] + tempCoefTx[count];
140             }
141         }
142     }
143     for (k = 0; k < nTime; k++)//nTime
144     {
145         for (j = 0; j < nSpatial; j++)//nSpatial
146         {
147             for (i = 0; i < rows; i++)
148             {
149                 tempCoefTy[i] = coefTy[i][j];
150             }
151             y_fit[j][k] = tempCoefTy[0];
152             for (count = 1; count <= rows-1; count++)
153             {
154                 y_fit[j][k] = y_fit[j][k]*timeFix[k] + tempCoefTy[count];
155             }
156         }
157     }
158
159 ////////////////////////////////////////////////////////////////////////////
160 // Begin tongue movement
161
162 Message("\n---------- Begin Tongue Movement ----------\n");
163   x =0;
164   tt = time/0.0008-1;
165     begin_f_loop(f,tf)
166     {
167       f_node_loop(f,tf,n)
168       {
169         v = F_NODE(f,tf,n);
170         if (NODE_POS_NEED_UPDATE (v))
171         {
172           NODE_POS_UPDATED(v);
173           NV_D(displ, =, x_fit[nk[x]-1][tt]/100, y_fit[nk[x]-1][tt]/100, 0.0);
174           NV_V(NODE_COORD(v),=,displ);
175           x++;
176         }
177       }
```

```
178     }
179     end_f_loop(f,tf)
180     Message("\n---------- END_TimeStep :): %d ----------\n", tt);
181 }
182 
183 /////////////////////////////////////////////////////////////////////////////
184 
185 DEFINE_GRID_MOTION(tongueOffset,domain,dt,time,dtime)
186 {
187   //Fluent variables declaration
188   Thread *tf = DT_THREAD(dt);
189   face_t f;
190   Node *v;
191   real NV_VEC(A);
192   int n;
193   real NV_VEC(displ2);
194 
195   //Algorithm variables declaration
196   int i, j, k, x, tt, nk2[nSpatial], count;
197   double timeFix[nTime], spatialFix[nSpatial];
198   double tempCoefyOffset[cols], tempCoefxOffset[cols], tempCoefTxOffset[rows],
        tempCoefTyOffset[rows];
199 
200 /////////////////////////////////////////////////////////////////////////////
201     //Declare matrices
202     double coefxOffset[rows][cols];
203     double coefyOffset[rows][cols];
204     double coefTxOffset[cols][nSpatial];
205     double coefTyOffset[cols][nSpatial];
206     double x_fitOffset[nSpatial][nTime];
207     double y_fitOffset[nSpatial][nTime];
208 
209 /////////////////////////////////////////////////////////////////////////////
210     //Call and store coefyOffset
211     file4=fopen("coefyOffset.txt", "r");
212     for(i = 0; i < rows; i++)
213     {
214         for(j = 0; j < cols; j++)
215         {
216             if (!fscanf(file4, "%lf", &coefyOffset[i][j]))
217             {
218                 break;
219             }
220         }
221     }
222     fclose(file4);
223 
224     //Call and store coefxOffset
```

```
225     file5=fopen("coefxOffset.txt", "r");
226     for(i = 0; i < rows; i++)
227     {
228         for(j = 0; j < cols; j++)
229         {
230             if (!fscanf(file5, "%lf", &coefxOffset[i][j]))
231             {
232               break;
233             }
234         }
235     }
236     fclose(file5);
237 
238         //Call and store parameters k
239     file6=fopen("k2.txt", "r");
240     for(i = 0; i < nSpatial; i++)
241     {
242             if (!fscanf(file6, "%d", &nk2[i]))
243             {
244               break;
245             }
246     }
247     fclose(file6);
248 
249 ////////////////////////////////////////////////////////////////////////////
250     //Define fix vectors linspaces
251     for(i=0;i<nTime;i++)
252     {
253         timeFix[i] = (double)(i) / ((double)(nTime)-1.0);
254     }
255     for(i=0;i<nSpatial;i++)
256     {
257         spatialFix[i] = (double)(i) / ((double)(nSpatial)-1.0);
258     }
259 
260 ////////////////////////////////////////////////////////////////////////////
261     // Eval polynom spatial
262     for (k = 0; k < nSpatial; k++)
263     {
264         for (i = 0; i < cols; i++)
265         {
266             for (j = 0; j < rows; j++)
267             {
268                 tempCoefxOffset[j] = coefxOffset[i][j];
269             }
270             coefTxOffset[i][k] = tempCoefxOffset[0];
271             for (count = 1; count <= cols-1; count++)
272             {
```

```
273                 coefTxOffset[i][k] = coefTxOffset[i][k]*spatialFix[k] +
    tempCoefxOffset[count];
274             }
275         }
276     }
277     for (k = 0; k < nSpatial; k++)
278     {
279         for (i = 0; i < cols; i++)
280         {
281             for (j = 0; j < rows; j++)
282             {
283                 tempCoefyOffset[j] = coefyOffset[i][j];
284             }
285             coefTyOffset[i][k] = tempCoefyOffset[0];
286             for (count = 1; count <= cols-1; count++)
287             {
288                 coefTyOffset[i][k] = coefTyOffset[i][k]*spatialFix[k] +
    tempCoefyOffset[count];
289             }
290         }
291     }
292
293 ////////////////////////////////////////////////////////////////////////////
294     // Eval polynom temporal
295     for (k = 0; k < nTime; k++)//nTime
296     {
297         for (j = 0; j < nSpatial; j++)//nSpatial
298         {
299             for (i = 0; i < rows; i++)
300             {
301                 tempCoefTxOffset[i] = coefTxOffset[i][j];
302             }
303             x_fitOffset[j][k] = tempCoefTxOffset[0];
304             for (count = 1; count <= rows-1; count++)
305             {
306                 x_fitOffset[j][k] = x_fitOffset[j][k]*timeFix[k] +
    tempCoefTxOffset[count];
307             }
308         }
309     }
310     for (k = 0; k < nTime; k++)//nTime
311     {
312         for (j = 0; j < nSpatial; j++)//nSpatial
313         {
314             for (i = 0; i < rows; i++)
315             {
316                 tempCoefTyOffset[i] = coefTyOffset[i][j];
317             }
```

```
318             y_fitOffset[j][k] = tempCoefTyOffset[0];
319             for (count = 1; count <= rows-1; count++)
320             {
321                 y_fitOffset[j][k] = y_fitOffset[j][k]*timeFix[k] +
    tempCoefTyOffset[count];
322             }
323         }
324     }
325
326 ////////////////////////////////////////////////////////////////////////////
327 // Begin tongue's offset movement
328
329 Message("\n---------- Begin Tongue Offset Movement----------\n");
330   x =0;
331   tt = time/0.0008-1;
332       begin_f_loop(f,tf)
333     {
334       f_node_loop(f,tf,n)
335       {
336         v = F_NODE(f,tf,n);
337         if (NODE_POS_NEED_UPDATE (v))
338         {
339           NODE_POS_UPDATED(v);
340           NV_D(displ2, =, x_fitOffset[nk2[x]-1][tt]/100, y_fitOffset[nk2[x
    ]-1][tt]/100, 0.0);
341           NV_V(NODE_COORD(v),=,displ2);
342           x++;
343         }
344       }
345     }
346     end_f_loop(f,tf)
347   Message("\n---------- END_TimeStep :): %d ----------\n", tt);
348 }
```

Appendix: UDF used in ANSYS Fluent for simpler geometries

C.1 Model 1

```
#include "udf.h"
#include "dynamesh_tools.h"

DEFINE_CG_MOTION(mod1, dt, vel, omega, time, dtime)
{
real v; // create real variable for linear velocity
v = 0.02; // assign value
vel[0] = v;
Message("%g %g\n",time,v);//print to console the angular velocity
}
```

C.2 Model 2

```
#include "udf.h"
#include "dynamesh_tools.h"

DEFINE_CG_MOTION(mod2,dt,vel,omega,time,dtime)
{
  real w; // create real variable for angular velocity
  w = 1.09; //rad / s
  omega[2] = w*time; //Assign new angle omega to fluent variable
  Message("%g %g\n",time,omega[2]); //print to console the angular velocity
}
```

Appendix: Tracking of food bolus' centroid from dMRI images

```
1
2  /*
3  Tongue size 72.827 mm
4   dt = 0.0178
5  76 px horizontal
6   -> 0.9582 ~ 1 mm / px
7  */
8
9  clear all
10 clc
11
12 filename1 = ('MRI/pb_0066_0');
13
14 for t = 576:740
15     filename2 = '.dcm';
16     tt = num2str(t);
17     filename = strcat(filename1,tt,filename2);
18     Idcm = dicomread(filename);
19     I = uint8(255 * mat2gray(Idcm));
20     subplot(1,2,1)
21     imshow(I)
22     str = sprintf('Original Image');
23     title(str)
24
25     figure(1);
26     hax = subplot(1,2,2);
27     Ibw = im2bw(I,0.7);
28     imshow(Ibw)
29     Ibw = imfill(Ibw,'holes');
30     Ilabel = bwlabel(Ibw);
31     stat = regionprops(Ilabel,'centroid');
32     imshow(I);
33     title('Centroid Image')
```

```
34      hold on
35
36      if numel(stat) > 1
37          dist = zeros(numel(stat),1);
38          for x = 1: numel(stat)
39              dist(x,:) = pdist([valAnt;stat(x).Centroid],'euclidean');
40          end
41          [val, xnew] = min(dist);
42          plot(stat(xnew).Centroid(1),stat(xnew).Centroid(2),'ro');
43      else
44          xnew = 1;
45           plot(stat(xnew).Centroid(1),stat(xnew).Centroid(2),'ro');
46      end
47
48      valAnt = stat(xnew).Centroid;
49
50      pause(0.1)
51  end
```

Acquisition of contour from the masked region

E.1 Algorithm to acquire the red-masked region

```
% prepare workspace
clc
clear all

for t = 1:140;

filenum = sprintf('%03d',t);%declare file number
filename = strcat('images2\PIVlab_out_',filenum,'.jpg');%declare file location
    and name

[rgbImage, storedColorMap] = imread(filename);% read image, store in rgbImage
rgbImage = rgbImage(303:1300,728:2150,:); % Crop image
[rows, columns, numberOfColorBands] = size(rgbImage); % extract image
   properties
% figure, imshow(rgbImage); %debugging

[bw, maskedimage] = createMask(rgbImage); % call function CreateMask
% figure, imshow(bw); %debugging

[B, L] = bwboundaries(bw, 'noholes'); %create boundarie aroung not zero
   objetcs
% hold on % debugging

% assign size of each boundary to an element of array n
for k = 1:length(B)
    boundary = B{k};
    n(k) = size(boundary,1);
end

boundaryMax = B{find(max(n))}; % find max n which indicates the longest
```

```
    boundary, i.e. the tongue.
28
29 boundaryMax = boundaryMax(1:1800,:);% crop tongue boundary
30 % plot(boundaryMax(:,2),-boundaryMax(:,1),'r.'); % debugging
31 % hold on
32
33 % noise in the boundary is found, therefore, we eliminate points where
34 % function is no viable. (two or more 'y' to a single 'x')
35 xx = boundaryMax(:,2); % auxiliar variable
36 binrange = min(xx):max(xx); % define range of xx
37 doubleCount = histc(xx,binrange); % create a histogram identify multiple 'x'
    with same value
38 repeatedVal = binrange(find(doubleCount>1)); % extract repeated values
39
40 % search for 'y' in repeated values and select the minimum 'y'.
41 for ii = 1:length(repeatedVal)
42 %     ii = 1; % debugging
43     repeatedRange = find(xx == repeatedVal(ii)); % compare xx with repeated
    values and store position.
44     maxY = min(boundaryMax(repeatedRange,1)); % search for positions and
    select min.
45     replaceWhere = find(boundaryMax(repeatedRange,1) ~= maxY); % find position
     where 'y' has several 'x'
46 %     plot(ones(size(deleteWhere)),boundaryMax(repeatedRange(deleteWhere),1),'
    b+','MarkerSize',4);
47 %     % debugging
48     boundaryMax(repeatedRange(replaceWhere),1) = maxY;% assign only one value
    for repeated y
49 end
50
51 % plot(boundaryMax(:,2),-boundaryMax(:,1));%plot boundary
52
53 pxscale = 0.0411; %997 px 41 mm
54
55 xx1(t) = max(boundaryMax(:,2))*pxscale;
56 yy2(t,:) = {unique(smooth(xx,-boundaryMax(:,1),0.1,'rloess'))*pxscale};
57
58 end
```

E.2 Complementary auto-generated function

```
1 function [BW,maskedRGBImage] = createMask(RGB)
2 %createMask  Threshold RGB image using auto-generated code from
    colorThresholder app.
3 %  [BW,MASKEDRGBIMAGE] = createMask(RGB) thresholds image RGB using
4 %  auto-generated code from the colorThresholder App. The colorspace and
5 %  minimum/maximum values for each channel of the colorspace were set in the
```

```
%  App and result in a binary mask BW and a composite image maskedRGBImage,
%  which shows the original RGB image values under the mask BW.

% Auto-generated by colorThresholder app on 01-Apr-2018
%------------------------------------------------------


% Convert RGB image to chosen Y'CBCR
RGB = im2double(RGB);
cform = makecform('srgb2lab', 'AdaptedWhitePoint', whitepoint('D65'));
I = applycform(RGB,cform);

% Define thresholds for channel Y based on histogram settings
channel1Min = 0.000;
channel1Max = 100.000;

% Define thresholds for channel CB based on histogram settings
channel2Min = 18.811;
channel2Max = 80.070;

% Define thresholds for channel CR based on histogram settings
channel3Min = -107.760;
channel3Max = 27.815;

% Create mask based on chosen histogram thresholds. If outside
% thresholds then 0. Otherwise, 1.
BW = (I(:,:,1) >= channel1Min ) & (I(:,:,1) <= channel1Max) & ...
     (I(:,:,2) >= channel2Min ) & (I(:,:,2) <= channel2Max) & ...
     (I(:,:,3) >= channel3Min ) & (I(:,:,3) <= channel3Max);

% Initialize output masked image based on input image.
maskedRGBImage = RGB;

% Set background pixels where BW is false to zero.
maskedRGBImage(repmat(~BW,[1 1 3])) = 0;
```

Appendix: Technical drawings of the experimental bench set up